

Comprehensive language–image pre-training for 3D medical image understanding

Tassilo Wald^{1,2†} Ibrahim Ethem Hamamci^{1†} Yuan Gao^{1†} Sam Bond-Taylor¹ Harshita Sharma¹
 Maximilian Ilse¹ Cynthia Lo¹ Olesya Melnichenko¹ Anton Schwaighofer¹
 Noel C. F. Codella¹ Maria Teodora Wetscherek^{1,3} Klaus H. Maier-Hein^{2,4} Panagiotis Korfiatis⁵
 Valentina Salvatelli¹ Javier Alvarez-Valle¹ Fernando Pérez-García^{1*}

¹Microsoft ²German Cancer Research Center (DKFZ)

³Department of Radiology, University of Cambridge and Cambridge University Hospitals NHS Foundation Trust

⁴Pattern Analysis and Learning Group, Heidelberg University Hospital ⁵Department of Radiology, Mayo Clinic

Abstract

Vision–language pre-training, i.e., aligning images with paired text, is a powerful paradigm to create encoders that can be directly used for tasks such as classification, retrieval, and segmentation. In the 3D medical image domain, these capabilities allow vision–language encoders (VLEs) to support radiologists by retrieving patients with similar abnormalities, predicting likelihoods of abnormality, or, with downstream adaptation, generating radiological reports. While the methodology holds promise, data availability and domain-specific hurdles limit the capabilities of current 3D VLEs.

*In this paper, we overcome these challenges by injecting additional supervision via a report generation objective and combining vision–language with vision-only pre-training. This allows us to leverage both image-only and paired image–text 3D datasets, increasing the total amount of data to which our model is exposed. Through these additional objectives, paired with best practices of the 3D medical imaging domain, we develop the **Comprehensive Language–Image Pre-training (COLIPRI)** encoder family. Our COLIPRI encoders achieve state-of-the-art performance in report generation, semantic segmentation, classification probing, and zero-shot classification. The model is available at <https://huggingface.co/microsoft/colipri>.*

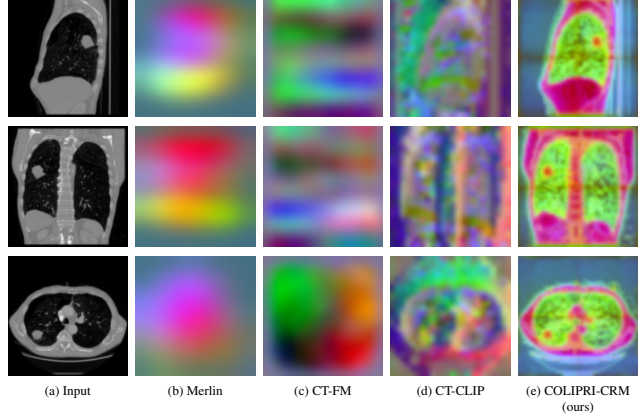


Figure 1. **Principal component analysis (PCA) maps of dense 3D features** obtained from (a) a CT scan with a lung mass using different encoders. Compared to the baseline methods (b)(c)(d), our COLIPRI-CRM encoder (e) generates sharper and more coherent features. The dense embeddings have sizes $7 \times 7 \times 10$ (b), $24 \times 24 \times 8$ (c), $24 \times 24 \times 24$ (d) and $48 \times 48 \times 48$ (e), and are interpolated here using bicubic interpolation for visualisation purposes. The sagittal (top), coronal (middle) and axial (bottom) slices of the 3D scan are centred on the lung mass. The Comprehensive Language–Image Pre-training (COLIPRI) (e) map was computed from the input resampled to 1 mm isotropic, cropped and padded to $384 \times 384 \times 384$, using a sliding window of size $192 \times 192 \times 192$.

1. Introduction

Contrastive language–image pre-training (CLIP) [36] has established itself as one of the strongest paradigms to learn general-purpose image and text representations. Aside from

[†]Work done during an internship at Microsoft Research Cambridge.

* Corresponding author: fperezgarcia@microsoft.com.

being a solid starting point for adaptation to downstream tasks of interest [14, 27], having language-aligned vision embeddings allows leveraging natural language for open-set classification [36] and open-set segmentation [58].

In 3D medical imaging, this training paradigm is especially relevant as every image acquired in a clinical setting is accompanied by a report, making this kind of paired data abundant in hospitals. The reports associated with the images offer (weak) supervision and enable zero-shot tasks for clinical support, such as image-to-report retrieval or open-set abnormality classification.

Despite these promises, the field of vision–language pre-training with medical images is not as mature as its general-domain counterpart. While CLIP [36], Perception Encoder [7], or SigLIP 2 [45] are well established in the general domain, 3D medical vision–language encoders (VLEs) have only recently started to garner attention [5, 15]. We believe that this can be attributed to two key issues: 1) the lack of large, publicly available, paired datasets in the medical domain and 2) domain- and modality-specific methodological and engineering hurdles.

Currently, the largest publicly available 3D datasets with image–report pairs reach a combined size of about 78k image–report pairs (Tab. A.1), which is far from the 400 million image–text pairs which CLIP [36] was trained on, and even further from the 12 billion alt-texts [9] used to train SigLIP 2 [45]. However, the relatively large number of available unpaired images has the potential to substantially increase the amount of overall usable data, when leveraged through self-supervised learning (SSL) (Tab. A.1). In this work, we address the above issues by demonstrating how to successfully adapt a vision–language pre-training approach to the 3D medical imaging domain, using both image-only and image–text open-access chest CT datasets.

The number of voxels in 3D medical images is orders of magnitude larger than the number of pixels in images from the general domain and 2D medical images. For example, a typical chest CT volume may be composed of $512 \times 512 \times 320$ voxels, making it difficult to use entire images in native resolution during training due to excessive VRAM requirements. A whole-body CT scan would be even larger, with over a thousand axial slices acquired. Due to the large size, it is common to either train with crops of images [34, 37] or downsampled images [5, 15]. Cropping may complicate CLIP-style training as clinical reports refer to the entire volume rather than just the field of view (FOV) of the sub-crop. Downsampling may discard image information that is crucial for detecting certain abnormalities, in particular small ones.

In this work, we improve the state of the art in 3D medical vision–language models by leveraging best practices of the 3D medical imaging domain and introducing inductive biases aimed at making the most of the available data. Our

contributions can be summarised as follows:

1. We investigate key design choices of the CLIP training paradigm in the context of 3D medical imaging to extract the maximum value from the limited available vision–language data and propose a novel Opposite Sentence Loss (OSL) to enable zero-shot classification with short queries.
2. We increase the supervision gained from the medical report by introducing a radiology report generation (RRG) objective akin to CapPa [44].
3. We demonstrate that a vision-only self-supervised objective in conjunction with the CLIP objective [28, 30] allows to include image-only data into the training set and enables more localised supervision for dense downstream tasks.
4. We comprehensively evaluate the resulting models through zero-shot classification, classification probes, report generation, retrieval, and semantic segmentation, demonstrating that our COLIPRI-CRM models represent the new state of the art.

The model weights, code for inference, and multiple usage examples are available at <https://huggingface.co/microsoft/colipri>.

2. Related work

Contrastive vision–language models such as CLIP [36] have demonstrated that large-scale paired image–text data enables transferable multimodal representations. Later variants improved the contrastive objective [56], or proposed a language-generation objective [44, 50], with others including additional self-supervised objectives [28, 30, 45]. In parallel to this, self-supervised learning (SSL) methods [38, 59] were developed to learn general purpose features from unpaired images, achieving strong general-purpose visual features in natural imaging.

Compared to natural imaging, 3D medical imaging incurs much higher computational costs due to its higher dimensionality and faces stricter data access constraints, limiting the overall amount of available data. These factors have slowed the progress of 3D image SSL, with a recent benchmark [49] showing that features generated by most 3D SSL methods [40, 52, 60] improve either dense or global downstream tasks, but generally not both. For dense downstream tasks, MAEs [29, 48] remain the strongest pre-training method, yielding features that adapt well for 3D semantic segmentation.

Medical VLEs have largely focused on 2D chest X-rays with paired reports [3, 6, 18, 51]. Early work on 3D medical images focussed on adapting contrastive language-image pre-training to 3D settings [5, 15], incorporate anatomy-awareness [37], or auxiliary supervision through chest X-rays [8]. Despite increased interest in the field of 3D SSL [33, 53] and vision–language pre-training, a research

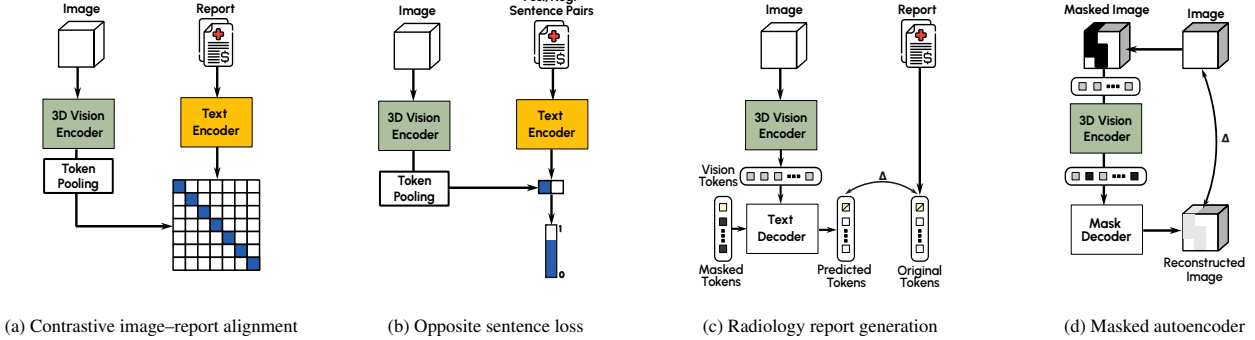


Figure 2. Combining (a) contrastive image–report pre-training, (b) the novel opposite sentence loss, (c) radiology report generation, and (d) masked autoencoders (MAEs) yields various versions of our Comprehensive Language–Image Pre-training (COLIPRI) vision–language encoders (VLEs).

gap remains between natural imaging and 3D medical imaging. Thus far, no work has combined self-supervised and vision–language objectives, nor has any research in the 3D imaging domain introduced a text generation objective.

3. Method

We present Comprehensive Language–Image Pre-training (COLIPRI), a multimodal pre-training framework that learns joint representations between 3D medical images and associated radiology reports. COLIPRI combines contrastive vision–language alignment, radiology report generation (RRG), masked image modelling (MIM), and a novel Opposite Sentence Loss (OSL) to produce 3D vision–language representations applicable to both global reasoning and dense prediction tasks (Fig. 2). We develop our models in stages, each adding a learning objective to assess the effects of each building block.

3.1. Report preprocessing

Radiological reports often contain details about all organs imaged, stating whether the findings are normal or not. Should abnormalities be present, they are explicitly named; however, when absent, the abnormalities are often not listed, as this would yield an excessive list of abnormalities a patient does not suffer from. The exceptions are typically abnormalities that might have prompted the imaging study in the first place. This style of reporting results in reports of substantial token sequence lengths, with the average *Findings* section of CT-RATE [15] being 243 tokens long when using the CXR-BERT tokeniser [6] (Fig. B.1). This is in stark contrast to Zhang et al. [57] or Radford et al. [36], which either sample a single sentence from the paired caption or whose datasets contain single-sentence captions.

To enable the objectives introduced later, we restructure each report with a large language model (LLM) into eight clinical subsections, denoted as C , assigning every sentence to one subsection. Additionally, we leverage the LLM to

create concise versions of all sentences s and to label them as *positive findings* (pathology present) s^+ or *negative findings* (normal) s^- . These preprocessed reports enable 1) language regularisation, 2) the OSL, and 3) our radiological report generation formulation. Details, prompts and examples are provided in Sec. A.3.

3.2. Adapting CLIP to 3D radiology

COLIPRI leverages the Primus-M transformer [47] architecture as the image encoder, and CXR-BERT [6] (pre-trained on chest X-rays) as the text encoder. The dense tokens of the vision and text encoders are aggregated through a multi-head attention-pooling mechanism to yield global representations. Due to different embedding dimensions of image and text encoders, the image embeddings are projected to the lower-dimensional text space, which can then be aligned using the CLIP paradigm [36].

In contrast to natural images, radiological reports describe findings across the entire scan, requiring a sufficiently large FOV for global context. However, large FOVs in 3D imaging increase the token sequence length, making training computationally expensive. We use inputs of size $160 \times 160 \times 160$ with an isotropic spacing of 2 mm, balancing FOV and token length for efficiency. We train with the default CLIP objective, which outperforms a sigmoid loss [55] in our setting.

The *Findings* section in radiology reports often resembles a long list, making the text encoder prone to overfitting to sentence order or stylistic cues rather than semantics. To counter this, we introduce two complementary text augmentations: 1) The *Sentence Shuffle* augmentation randomly permutes sentences within a report, discouraging reliance on order; 2) The *Short Sentence* augmentation replaces long-form reports with LLM-shortened statements with a given probability during training. This reduces the domain shift generated by training on long reports and running inference using brief zero-shot prompts (e.g., “{abnormality}

present” or “No {abnormality} present”). Additional ablations and detailed hyperparameters are provided in Sec. B.1.

3.2.1 Opposite Sentence Loss

Using the LLM-structured, shortened, and categorised reports (Sec. 3.1), we further reduce the training–inference domain shift with an Opposite Sentence Loss (OSL). Let x_i denote the image for case i , and let s_i^+ denote a *positive findings* sentence sampled from the report r_i . We create s_i^- , a negation of s_i^+ , via the template “No {sentence}.”. If s_i^+ originates from the report of case i then the sentence s_i^+ does correctly describe the image, yielding label $y_i = 1$. Additionally, for any clinical subsection of the current report that contains no positive findings, we draw *positive findings* sentences from the same subsection in other reports. These sampled positive findings do not describe the current image and therefore serve as negative examples, paired with their negated counterparts to form (s_i^+, s_i^-) pairs with supervision label $y_i = 0$. Let e_i^+ and e_i^- be the text embeddings of the positive and negated statement pair, and v_i the global image embedding. We compute a cosine similarity between image and text embeddings, followed by a temperature-scaled softmax over the pair and optimise a cross-entropy loss between probability p_i^+ and label y_i to maximise $\text{sim}(e_i^+ | v_i)$ if s_i^+ describes the image and minimises $\text{sim}(e_i^+ | v_i)$ if s_i^+ does not describe the image (described in Sec. B.4 and Algorithm 1). This trains the model in a short-prompt-manner and with statements of abnormality presence and absence, as used during zero-shot inference, explicitly learning to disambiguate presence vs. absence of findings. We combine our OSL objective with the CLIP objective, $\mathcal{L}_{\text{align}} = 0.5 \cdot \mathcal{L}_{\text{CLIP}} + 0.5 \cdot \mathcal{L}_{\text{OSL}}$, yielding our intermediate **COLIPRI-C** method (Tab. B.7).

3.3. Radiology report generation

To enrich the visual representations we introduce a radiology report generation (RRG) objective. This task aims to ensure that the vision encoder captures the complete semantic content of the associated report, rather than only discriminative cues required for contrastive pairing. Following Tschannen et al. [44], we evaluated two decoding modes during training: *causal captioning* and *parallel captioning*. In causal captioning mode, the decoder operates autoregressively, predicting each token conditioned on all preceding tokens, $p_{\text{causal}}(y_t | y_{<t}, \mathbf{v})$, where \mathbf{v} denotes the dense visual features and $y_{<t}$ the previously generated tokens. This setup enables sequential report generation akin to standard language modelling. In contrast, the parallel (masked) mode predicts all tokens simultaneously from a fully masked input, $p_{\text{parallel}}(y_t | \mathbf{M}, \mathbf{v})$, where \mathbf{M} denotes a mask applied to all text tokens. This formulation forces the text decoder to use the dense visual representations \mathbf{v} rather

than previously generated text $y_{<t}$. We found that *parallel captioning* yields better results, and hence discarded *causal captioning* in our final COLIPRI models (see Tab. B.5).

We implement RRG using a lightweight EVA-02 [13] transformer decoder connected to the vision encoder via cross-attention. To mitigate order ambiguity inherent to free-form clinical text, we leverage the LLM-structured reports introduced in Sec. 3.1, where each sentence is assigned to one of eight clinical subsections. These structured reports reduce positional uncertainty by providing a consistent ordering of findings across studies, ensuring that the decoder learns to model clinical content rather than author-specific stylistic variation. During decoding, clinical subsection headers are kept unmasked to guide generation and preserve report semantics. The RRG objective is optimised jointly with the contrastive and OSL objectives: $\mathcal{L}_{\text{VLM}} = 0.5 \cdot \mathcal{L}_{\text{CLIP}} + 0.5 \cdot \mathcal{L}_{\text{OSL}} + \lambda_{\text{RRG}} \mathcal{L}_{\text{RRG}}$ on paired image–report batches, yielding our intermediate **COLIPRI-CR** method (see Tab. B.7).

3.4. Including vision-only self-supervision

While multimodal pre-training provides strong representations for global reasoning tasks, such methods rely on paired data and often underperform on dense, spatially localised tasks [31]. To improve the spatial quality of the learned representations, we include a vision-only masked autoencoder (MAE) objective [16].

Given the lack of advanced dense SSL methods such as iBOT [59] or DINOv3 [38] in 3D medical imaging, MAE pre-training provides a straightforward and effective choice. It reconstructs missing volumetric patches from context, encouraging the model to learn dense feature representations that complement the global semantic alignment achieved by the CLIP and RRG objectives. To provide a strong initialisation, we pre-train a Primus-M vision encoder first, leveraging the nnSSL framework [49], before joint multimodal training.

We implement MAE as a lightweight decoder attached to the vision encoder to reconstruct masked patches in voxel space using a mean-squared-error loss. To avoid interference of the vision-only masking with the vision–language objectives, we use a training scheme that alternates between vision-only and vision–language objectives, optimising either $\mathcal{L}_{\text{Align}} = 0.5 \cdot \mathcal{L}_{\text{CLIP}} + 0.5 \cdot \mathcal{L}_{\text{OSL}}$ or $\mathcal{L}_{\text{VO}} = \lambda_{\text{MAE}} \mathcal{L}_{\text{MAE}}$. This design allows benefitting from paired supervision when available, while still leveraging the often much larger image-only datasets such as NLST [41].

Finally, since the vision-only objective does not require a global FOV, we sample high-resolution (1 mm isotropic) and default-resolution (2 mm isotropic) sub-crops during MAE pre-training. This exposes the encoder to finer spatial detail, reducing the shift between pre-training and high-resolution downstream data. The resulting com-

bination of COLIPRI-C with the MAE objective yields our COLIPRI-CM VLE. Further, combining all of the introduced objectives (CLIP, OSL, RRG, and MAE) yields our final VLE, COLIPRI-CRM (Tab. B.7).

4. Experiments

We pre-train our COLIPRI models on CT-RATE [15] (for the vision-language and vision-only objectives) and NLST [41] (for the vision-only objective). Dataset and training details are presented in Secs. A and B. The resulting encoders are evaluated on multiple unimodal (semantic segmentation, multilabel classification) and multimodal (zero-shot classification, report generation, retrieval) downstream tasks.

4.1. Classification and report generation

Classification performance is evaluated on a withheld test set of CT-RATE and on the publicly available subset of RAD-ChestCT [12], which comprises 3.6k chest CT volumes with 16 multi-abnormality labels that can be derived from the original CT-RATE abnormality classes. We evaluate linear classification probes, as well as zero-shot classification performance on both datasets (Sec. C.2).

As an additional global task, we evaluate the quality of the frozen image encoder embeddings for report generation. To do this, we follow the LLaVA framework [25], with image tokens passed through a two-layer multilayer perceptron (MLP) to integrate them into the language space of the Qwen2.5 1B base model [43]. We focused on generating the *Findings* section of each report with details provided in Sec. C.4. To evaluate the clinical accuracy of generated reports, we use the text classifier trained by Hamamci et al. [15] based on RadBERT [54]. We also use the RadFact-CT (+/-) and RadFact-CT (+), variants of RadFact [4] with CT-specific system prompts and few-shot examples as described in Sec. C.1.

As baselines, we compared our method against established CT models, namely CT-CLIP [15], CT-FM [32] (both trained on chest CT datasets), and Merlin [5] (trained on abdominal CTs, but we found it to be a competitive baseline for chest CT report generation). For zero-shot classification, we additionally compare against fVLM [37] and BIUD [8]. We also compare our method against two 2D VLE which included CT slices in their pre-training data, namely Med-ImageInsight [10], a general medical imaging model, and Curia [11], a radiology-specific model. We evaluate linear and zero-shot classification for the two 2D models by averaging the pixel values of a volume along the axial dimension and encoding the resulting average slice (we also tried max, mean, standard deviation and median pooling [10] but found that slice averaging works best). For RRG, we instead encode all axial slices independently and perform max pooling of the embeddings.

4.2. Semantic segmentation

To evaluate the quality of the vision encoder for dense tasks, we measure 3D medical image segmentation performance after fine-tuning the encoder. In this setting, we compare against a Primus-M [47] encoder trained from scratch, as well as a state-of-the-art MAE-pre-trained [49] Primus-M encoder trained on CT-RATE and NLST (Sec. A.1.1). Additionally, we compare with the default nnU-Net [20] and ResEnc-L [21] CNN encoders trained from scratch as references. All training runs are conducted using the nnU-Net framework [20], with all of the encoders being fine-tuned in a short (37.5k steps) and a long (250k steps) schedule, using the learning rate schedule described in Wald et al. [49], with the peak learning rate reduced to 10^{-4} . To remain partially in distribution, we chose to focus on segmentation datasets with targets in the chest region or the upper abdomen, a FOV that is often visible during pre-training. On each segmentation dataset, we train a five-fold cross-validation. As datasets, we choose

1. **LiTS** [39] ($N = 131$), task 3 of the Medical Segmentation Decathlon (MSD), which contains segmentations for liver and liver tumours.
2. **Lung** [39] ($N = 64$), task 6 of the MSD, which contains cases of primary lung cancers.
3. **HVS** [39] ($N = 303$), task 8 of the MSD, which focuses on segmenting hepatic vessels and adjacent tumours.
4. **KiTS23** [17] ($N = 489$), a more recent dataset focused on segmenting tumours, cysts, and kidneys.

We use the Dice similarity coefficient (DSC) averaged across all foreground classes to report segmentation performance.

5. Results and discussion

5.1. Classification probes

We evaluate the quality of our COLIPRI vision encoders and other baseline vision encoders using classification probes on CT-RATE and RAD-ChestCT (Tab. 1).

Compared to reference values from the literature, we observe that our probing setup is largely superior to previous probe setups, yielding AUROC values of above 80% for the majority of baseline methods (vs. approx. 75% reported in the original works) as well as our own encoders. This likely originates from our training setup, which uses multiple probes with different learning rates and token pooling methods, selecting the best probe on the validation split for testing. Moreover, not all of our token aggregation schemes are linear as some include a light-weight attention pooling block, which is more flexible than a linear layer. We believe this multi-probe scheme to be more suited for comparison due to its robustness to hyperparameter selection, and its independence of the existence or quality of global-pooling layers attached to the vision backbones. The only excep-

Table 1. Classification probing results. We compare the embedding quality of our vision encoders against publicly available baselines. Our COLIPRI-CM and COLIPRI-CRM encoders yield the best classification results, exceeding all baselines on both datasets across all metrics. The metrics for “CT-CLIP (reported)” are from Shui et al. [37]. Differences in performance with the metrics we computed using the released checkpoints may be due to configuration issues. Hence, we report both sets of values for fairness and clarity. We report macro average and 95% confidence intervals (CIs) based on 100 bootstrap samples. **Bold** indicates best performance for that metric, or overlapping CIs with best. AUPRC: area under the precision-recall curve; AUROC: area under the receiver operating characteristic curve.

Model	CT-RATE		RAD-ChestCT	
	AUPRC	AUROC	AUPRC	AUROC
MI2 (2D)	19.70	50.52	27.94	52.25
Curia (2D)	45.93	78.01	39.23	65.73
CT-CLIP	25.96 [24.74, 27.48]	61.21 [60.02, 62.45]	28.77 [28.23, 29.49]	54.05 [53.12, 55.01]
CT-CLIP (reported)	-	75.1	-	64.7
CT-FM	53.54 [51.93, 55.02]	82.14 [81.44, 82.82]	42.41 [41.66, 43.21]	68.49 [67.97, 69.15]
MAE	53.79 [52.55, 55.39]	82.70 [82.02, 83.31]	45.24 [44.71, 46.07]	71.20 [70.60, 71.71]
Merlin	54.81 [53.19, 56.81]	82.62 [81.84, 83.30]	45.30 [44.45, 46.20]	70.91 [70.30, 71.48]
COLIPRI-C	55.13 [53.59, 56.80]	82.63 [81.87, 83.34]	46.33 [45.61, 47.37]	71.20 [70.65, 71.78]
COLIPRI-CR	57.44 [56.00, 59.02]	83.50 [82.90, 84.04]	48.28 [47.44, 49.12]	72.78 [72.16, 73.42]
COLIPRI-CM	61.52 [60.14, 63.03]	86.15 [85.66, 86.78]	51.79 [50.93, 52.76]	76.16 [75.65, 76.61]
COLIPRI-CRM	61.28 [59.59, 63.10]	86.12 [85.52, 86.85]	52.55 [51.72, 53.65]	76.57 [76.08, 77.18]

tion for this performance increase is the CT-CLIP encoder, which curiously performs worse in our experiments. This might be due to a potential configuration issue, hence we additionally report the results from Shui et al. [37] for the metrics in common.

Our COLIPRI models exceed all baselines across all metrics and datasets, with COLIPRI-CM and COLIPRI-CRM representing the strongest encoders for classification. In particular, COLIPRI-CRM increases by 6 points AUPRC and 3.5 points AUROC over the best-performing baseline Merlin. The inclusions of our RRG and MAE objectives increases classification performance, likely due to the added objectives serving as regularisation.

5.2. Zero-shot classification

For all VLEs, we report the zero-shot classification performance on CT-RATE and RAD-ChestCT in Tab. 2, using a short-form prompting scheme for our models (Sec. A.4). Values for some baselines are taken from the fVLM paper [37]. However, in their work, results are reported for only 16 of the 18 abnormalities in CT-RATE, excluding the non-localisable ‘Lymphadenopathy’ and ‘Medical Material’ as they are not associated with an organ¹, which is a limitation of fVLM. We report results including all abnormalities in Tab. D.1.

Our COLIPRI-CM and COLIPRI-CRM encoders outperform all baselines on CT-RATE, while the COLIPRI-C and COLIPRI-CR encoders perform worse. When eval-

¹<https://github.com/alibaba-damo-academy/fvml/issues/12#issuecomment-3283463870>

Table 2. Zero-shot classification results. We report macro AUPRC and AUROC excluding ‘Medical Material’ and ‘Lymphadenopathy’ to be consistent with [37]. An extended version of this table with all abnormalities is provided in Tab. D.1. Across both metrics and datasets, our VLEs exceed the state of the art using short prompts, without relying on segmentation masks at inference as fVLM does. We report mean and 95% CIs based on 100 bootstrap samples. **Bold** indicates best performance for that metric, or overlapping CIs with best.

Model	CT-RATE		RAD-ChestCT	
	AUPRC	AUROC	AUPRC	AUROC
MedImageInsight	18.80	49.36	26.32	48.82
Curia	19.18	50.17	26.84	50.13
CT-CLIP	-	70.4*	-	63.2*
BIUD	-	71.3*	-	62.9*
Merlin	-	72.8*	-	64.4*
fVLM	-	77.8*	-	68.0*
COLIPRI-C	43.81 [42.9, 45.2]	76.25 [75.5, 77.2]	40.98 [40.3, 41.8]	69.12 [68.6, 69.7]
COLIPRI-CR	44.70 [43.7, 46.5]	76.41 [75.7, 77.2]	39.38 [38.7, 40.1]	67.30 [66.6, 68.1]
COLIPRI-CM	50.32 [48.7, 51.8]	80.52 [79.7, 81.4]	43.26 [42.5, 44.3]	72.05 [71.4, 72.7]
COLIPRI-CRM	49.39 [48.3, 51.3]	79.81 [79.2, 80.7]	44.48 [43.7, 45.4]	73.23 [72.6, 73.8]

* Values are taken from [37].

Table 3. The Opposite Sentence Loss (OSL) enables short-form zero-shot classification. Validation-set results with and without the OSL. Without the OSL, zero-shot classification with short prompts performs substantially worse than using a long-form, more native prompting style.

Prompt Style	Native		Short	
	AUPRC	AUROC	AUPRC	AUROC
COLIPRI-CRM	51.17	81.91	50.70	81.66
without OSL	47.48	80.48	39.08	74.09

ated on RAD-ChestCT, COLIPRI-CRM generalises better than our other encoders or fVLM, with fVLM decreasing 10 points in AUROC on RAD-ChestCT.

Comparing the zero-shot classification performance of encoders with and without our OSL (Tab. 3), we observe that including the loss closes the gap between a native, longer-form prompting scheme where we average the embeddings of 50 randomly sampled reports with the abnormality and 50 without, versus the short-form prompts where we query with “{abnormality} present” and “no {abnormality} present”. This greatly improves the utility of the encoder because short queries are substantially easier to create than the ‘native’, longer-form queries.

5.3. Report generation

We evaluate the impact of our pre-training strategy on downstream RRG using both lexical and clinical metrics (Fig. 3, Tab. D.2). Across all lexical metrics (ROUGE-L, BLEU1, BLEU4, and METEOR) our COLIPRI-CRM encoder performs slightly better than the baselines, meaning that they all generate lexically accurate reports. However,

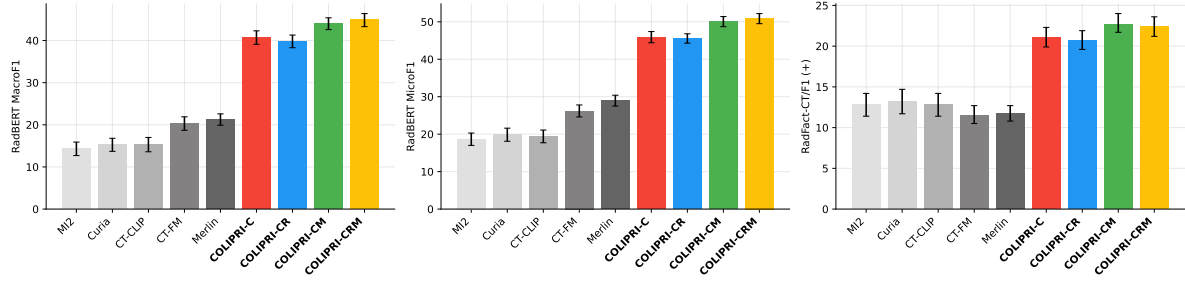


Figure 3. **Report generation results (summary).** Our COLIPRI vision encoders enable generating reports substantially better than the state of the art. In particular, the LLM trained on top of our models generates more accurate statements about abnormalities being present, as measured by RadFact-CT (+)/ F_1 and the RadBERT F_1 . The exact values are presented in Tab. D.2. RadFact-CT (+)/ F_1 : summary of logical precision and recall of positive findings (i.e., describing a present abnormality as judged by GPT-4o) [4]. We report median and 95% CIs (error bars) based on 500 bootstrap samples.

high lexical overlap does not necessarily imply clinically accurate reports [23].

When looking at clinical metrics, our COLIPRI vision encoders outperform all baselines by a very large margin. We use F_1 scores from the RadBERT classifier and RadFact-CT (+), which measure the correctness of medical entities and factual statements. Specifically, COLIPRI-CRM improves by 23 points in RadBERT Macro F_1 and by 9 points in RadFact-CT (+)/ F_1 over the strongest baseline, reflecting that the produced reports contain fewer omissions and more specific diagnostic statements. This demonstrates that our pre-training paradigm yields representations that encode more clinically relevant semantics. In absolute terms, however, the overall accuracy of generated reports for 3D medical is still low, with Macro F_1 -Scores of around 45% for the abnormalities measured by RadBERT and F_1 -scores of around 22% for all abnormalities as measured by RadFact-CT (+). When comparing the results of our methods, we observe that the COLIPRI-C and COLIPRI-CR exhibit slightly lower performance compared to the other encoders including MAE pre-training. Interestingly, the inclusion of the RRG objective appears to have a minimal impact on overall RRG performance, despite explicitly optimising embeddings to facilitate report generation. The inclusion of the MAE objective, on the other hand, appears to substantially improve performance. As such, we hypothesise that the MAE objective, which encourages the vision encoder to learn low-level semantic representations, better supports the LLaVA framework [25]. The RRG supervision might lead to more language-aligned features, which may result in the loss of more fine-grained features.

Comparing the values of RadFact-CT (+), which considers only statements mentioning the presence of abnormalities, and RadFact-CT (+/-), which considers statements about healthy organs and statements about abnormalities, reveals very different behaviour (see Tab. D.2). While our encoders reach substantially better metrics in the (+) set-

Table 4. **Report-to-image retrieval results.** Retrieval results on our CT-RATE test set, after deduplicating identical reports, yielding a total sample size of $N = 1493$. CT-CLIP retrieval values are taken from Hamamci et al. [15].

	R@1	R@5	R@10
CT-CLIP	-	2.90	5.00
COLIPRI-C	4.49	13.46	19.69
COLIPRI-CR	7.23	19.36	26.99
COLIPRI-CM	14.53	34.16	45.34
COLIPRI-CRM	15.27	35.10	46.01

ting, some of the baselines achieve slightly higher scores than our encoders as measured in the (+/-) setting. This is attributable to the vast imbalance of statements about presence vs. absence of abnormalities, with the latter dominating the metric. Thus, the inclusion of normal (negative) findings is an important but double-edged aspect of medical report generation. Since statements about the absence of abnormalities improve apparent completeness and boost (+/-) metrics, they can mask a low diagnostic sensitivity, as highlighted in our (+) results.

5.4. Retrieval

Report-to-image retrieval results on our CT-RATE test set are presented in Tab. 4. All our COLIPRI VLEs are substantially better in retrieving the associated image given a report. In particular, our COLIPRI-CRM VLE yields a R@5 of 35.1% compared against a R@5 of 2.9% of CT-CLIP, highlighting the strong multi-modal alignment of our encoders. Moreover, the inclusion of the RRG and MAE objectives positively benefit retrieval performance, with the MAE yielding larger performance improvements.

5.5. Segmentation

We evaluate semantic segmentation performance on the LiTS, Lung, HVS and KiTS23 datasets, against a baseline

Table 5. Segmentation fine-tuning results. Mean DSC results of five-fold cross-validation trained for 37.5k steps or 250k steps. Across all datasets, our COLIPRI-CM and COLIPRI-CRM vision encoders perform on par or better than the state-of-the-art (SOTA) pre-training method MAE, when adapted for downstream segmentation. We highlight the best short and long fine-tuning results of the same architecture in bold, and second best underlined.

Trainer	LiTS	Lung	HVS	KiTS23
References (250k steps)				
nnU-Net Default	80.09	70.32	68.38	86.04
nnU-Net ResEnc-L	81.60	70.34	67.73	88.17
Primus-M (37.5k steps)				
From scratch	74.39	62.74	64.67	78.90
MAE	<u>80.27</u>	67.12	67.10	85.34
COLIPRI-C	76.77	65.89	64.64	81.02
COLIPRI-CR	77.09	65.32	65.08	80.71
COLIPRI-CM	79.97	68.74	66.58	86.03
COLIPRI-CRM	80.46	68.98	67.05	85.79
Primus-M (250k steps)				
From scratch	79.75	69.11	65.34	86.25
MAE	<u>80.32</u>	67.46	<u>65.73</u>	87.46
COLIPRI-CRM	81.11	<u>67.56</u>	66.42	87.68

trained from scratch and an MAE pre-trained on NLST and CT-RATE at 1-mm and 2-mm isotropic resolutions, using the nnSSL framework [49] (Tab. 5).

In the short training regime of 37.5k steps, our encoders including MAE pre-training consistently exceed training from scratch, exceed or match the strong purely MAE pre-trained baseline. The encoders without the MAE objective also exceed training from scratch, but show lower segmentation performance, highlighting the importance of including the MAE objective for dense downstream task adaptation. This low performance of the COLIPRI-C and COLIPRI-CR models is not surprising, as it was shown that contrastive baselines struggle to surpass a baseline trained from scratch for segmentation tasks in Wald et al. [49].

When fine-tuning for 250k steps, our final COLIPRI-CRM model exceeds the pure MAE pre-training and improves for LiTS and KiTS, but decreases for Lung and HVS relative to the short fine-tuning schedule. For the Lung dataset, training from scratch yields better results than using pre-training. This is not uncommon as fine-tuning for longer may lead to overfitting and decreasing performance [49]. Comparing the nnU-Net default and ResEnc-L references with the results of the Primus-M encoder trained from scratch, it is clear that, on LiTS and KiTS, where Primus-M is close in performance to the CNN references, pre-training allows to exceed the default nnU-Net, while the gap to the ResEnc-L is not closed. This suggests that transformer encoders are generally still lagging behind their convolutional neural network (CNN) counterparts, indicating the need for transformer architectures with stronger segmentation capabilities.

5.6. Qualitative analysis

Aside from quantitative results, we provide a PCA visualisation of the 3D embeddings of Merlin, CT-FM, CT-CLIP, and our COLIPRI-CRM encoder, on a lung cancer case from the MSD Lung dataset (Fig. 1). The embedding resolution is very low for Merlin and CT-FM, providing hardly any semantic localisation. CT-CLIP yields embeddings of higher resolution, allowing features to be visually mapped from the input CT to the PCA map. However, the PCA map is inconsistent and noisy, and exhibits a strong bias towards absolute position within the scan, as visible through the anteroposterior green/red shift. On the other hand, our COLIPRI encoders yield higher-resolution embeddings, which are sharper and more consistent, allowing for clear recognition of the boundaries of the patient, lungs, and the abdominal organs, as well as the lung mass present in the right lung (on the left-hand side of the coronal and axial slice views).

5.7. Summary of the results

Our encoders learn clinically relevant features, as measured by the linear separability of features to abnormality classes (Sec. 5.1) and by our higher clinical accuracy in report-generation, yielding SOTA results in both aspects.

Moreover, our encoders show great text-to-image alignment, showing substantial improvements in report-to-image retrieval, and are sensitive to fine-grained similarity measurements, as evidenced by our SOTA zero-shot classification results (Sec. 5.2). While the former is an effect of our additional MAE and RRG supervision signals, the latter is enabled by our novel Opposite Sentence Loss (OSL), which teaches our text encoder to embed short statements in a semantically meaningful way. However, a substantial gap remains between classification probes and zero-shot classification, indicating potential for further improvement in alignment. Regarding dense tasks, our encoder including the MAE objective yield results that are better or on par with the current SOTA SSL pre-training method MAE (Sec. 5.5). Compared to SOTA CNNs, however, our transformer architecture still limits the performance of our encoders, yielding worse performance than ResEnc-L.

Across all our experiments, we find that our COLIPRI-CRM encoder provides embeddings that are potent in global tasks and is adaptable to dense downstream tasks, demonstrating the strength and versatility of our method.

6. Limitations and conclusion

Various limitations and opportunities for improvement remain, from technical and clinical points of view.

On the technical side, the inclusion of the radiology report generation (RRG) objective yields only slight improvements, indicating insufficiencies in the objective formula-

tion, and a large gap between classification probe and zero-shot classification highlights the need for better alignment.

On the clinical side, despite the improvements achieved by COLIPRI-CRM, the clinical performance metrics remain below the thresholds typically expected in clinical practice. We anticipate that training the model on a substantially larger and more diverse dataset would further enhance its performance. Additionally, a more comprehensive evaluation, stratified by clinical findings and patient characteristics, would be necessary to fully assess and demonstrate the model’s potential clinical utility.

In conclusion, COLIPRI achieves SOTA performance across all standard tasks, including classification, retrieval, segmentation, and report generation. Extensive evaluation on established benchmarks demonstrates consistent improvements over prior work, including stronger generalisation across datasets. These results confirm that COLIPRI advances the empirical frontier of the field and establishes a new performance baseline for the commonly studied tasks.

References

[1] Ibrahim M Alabdulmohsin, Xiaohua Zhai, Alexander Kolesnikov, and Lucas Beyer. Getting vit in shape: Scaling laws for compute-optimal model design. *Advances in Neural Information Processing Systems*, 36: 16406–16425, 2023. [15](#), [18](#)

[2] Yaël Balbastre, Kaidong Chai, Kabilar Gunalan, Fernando Pérez-García, Satrajit Ghosh, and Anastasia Yendiki. nifti-zarr-py: Implementation of the nifti-zarr specification in python, 2025. [13](#)

[3] Shruthi Bannur, Stephanie Hyland, Qianchu Liu, Fernando Pérez-García, Maximilian Ilse, Daniel C. Castro, Benedikt Boecking, Harshita Sharma, Kenza Bouzid, Anja Thieme, Anton Schwaighofer, Maria Wetscherek, Matthew P. Lungren, Aditya Nori, Javier Alvarez-Valle, and Ozan Oktay. Learning to exploit temporal structure for biomedical vision-language processing. In *Proceedings of the IEEE/CVF Conference on Computer Vision and Pattern Recognition (CVPR)*, pages 15016–15027, 2023. [2](#)

[4] Shruthi Bannur, Kenza Bouzid, Daniel C Castro, Anton Schwaighofer, Anja Thieme, Sam Bond-Taylor, Maximilian Ilse, Fernando Pérez-García, Valentina Salvatelli, Harshita Sharma, et al. Maira-2: Grounded radiology report generation. *arXiv preprint arXiv:2406.04449*, 2024. [5](#), [7](#), [23](#)

[5] Louis Blankemeier, Joseph Paul Cohen, Ashwin Kumar, Dave Van Veen, Syed Gardezi, Magda Paschali, Zhihong Chen, Jean-Benoit Delbrouck, Eduardo Reis, Cesar Truyts, Christian Bluethgen, Malte Jensen, Sophie Ostmeier, Maya Varma, Jeya Valanarasu, Zhongnan Fang, Zepeng Huo, Zaid Nabulsi, Diego Ardila, Wei-Hung Weng, Edson Amaro Junior, Neera Ahuja, Jason Fries, Nigam Shah, Andrew Johnston, Robert Boutin, Andrew Wentland, Curtis Langlotz, Jason Hom, Sergios Gatidis, and Akshay Chaudhari. Merlin: A Vision Language Foundation Model for 3D Computed Tomography, 2024. ISSN: 2693-5015. [2](#), [5](#), [13](#), [20](#)

[6] Benedikt Boecking, Naoto Usuyama, Shruthi Bannur, Daniel C Castro, Anton Schwaighofer, Stephanie Hyland, Maria Wetscherek, Tristan Naumann, Aditya Nori, Javier Alvarez-Valle, et al. Making the most of text semantics to improve biomedical vision–language processing. In *European conference on computer vision*, pages 1–21. Springer, 2022. [2](#), [3](#), [15](#)

[7] Daniel Bolya, Po-Yao Huang, Peize Sun, Jang Hyun Cho, Andrea Madotto, Chen Wei, Tengyu Ma, Jiale Zhi, Jathushan Rajasegaran, Hanoona Rasheed, Junke Wang, Marco Monteiro, Hu Xu, Shiyu Dong, Nikhila Ravi, Daniel Li, Piotr Dollár, and Christoph Feichtenhofer. Perception Encoder: The best visual embeddings are not at the output of the network, 2025. *arXiv:2504.13181 [cs]*. [2](#)

[8] Weiwei Cao, Jianpeng Zhang, Yingda Xia, Tony C. W. Mok, Zi Li, Xianghua Ye, Le Lu, Jian Zheng, Yuxing Tang, and Ling Zhang. Bootstrapping Chest CT Image Understanding by Distilling Knowledge from X-ray Expert Models. pages 11238–11247, 2024. [2](#), [5](#)

[9] Xi Chen, Xiao Wang, Soravit Changpinyo, AJ Piergiovanni, Piotr Padlewski, Daniel Salz, Sebastian Goodman, Adam Grycner, Basil Mustafa, Lucas Beyer, Alexander Kolesnikov, Joan Puigcerver, Nan Ding, Keran Rong, Hassan Akbari, Gaurav Mishra, Linting Xue, Ashish V Thapliyal, James Bradbury, Weicheng Kuo, Mojtaba Seyedhosseini, Chao Jia, Burcu Karagol Ayan, Carlos Riquelme Ruiz, Andreas Peter Steiner, Anelia Angelova, Xiaohua Zhai, Neil Houlsby, and Radu Soricu. PaLI: A jointly-scaled multilingual language-image model. In *The Eleventh International Conference on Learning Representations*, 2023. [2](#)

[10] Noel C. F. Codella, Ying Jin, Shrey Jain, Yu Gu, Ho Hin Lee, Asma Ben Abacha, Alberto Santamaría-Pang, Will Guyman, Naiteek Sangani, Sheng Zhang, Hoifung Poon, Stephanie Hyland, Shruthi Bannur, Javier Alvarez-Valle, Xue Li, John Garrett, Alan McMillan, Gaurav Rajguru, Madhu Maddi, Nilesh Vijayrania, Rehaan Bhimai, Nick Mecklenburg, Rupal Jain, Daniel Holstein, Naveen Gaur, Vijay Aski, Jenq-Neng Hwang, Thomas Lin, Ivan Tarapov, Matthew Lungren, and Mu Wei. MedImageInsight: An Open-Source Embedding Model for General Domain Medical Imaging, 2024. *arXiv:2410.06542 [eess]*. [5](#)

[11] Corentin Dancette, Julien Khlaut, Antoine Saporta, Hélène Philippe, Elodie Ferreres, Baptiste Callard,

Théo Danielou, Léo Alberge, Léo Machado, Daniel Tordjman, Julie Dupuis, Korentin Le Floch, Jean Du Terrail, Mariam Moshiri, Laurent Dercle, Tom Boeken, Jules Gregory, Maxime Ronot, François Legou, Pascal Roux, Marc Sapoval, Pierre Manceron, and Paul Hérent. Curia: A multi-modal foundation model for radiology, 2025. 5

[12] Rachel Lea Draelos, David Dov, Maciej A Mazurowski, Joseph Y. Lo, Ricardo Henao, Geoffrey D. Rubin, and Lawrence Carin. RAD-ChestCT Dataset, 2020. 5

[13] Yuxin Fang, Quan Sun, Xinggang Wang, Tiejun Huang, Xinlong Wang, and Yue Cao. Eva-02: A visual representation for neon genesis. *Image and Vision Computing*, 149:105171, 2024. 4

[14] Sachin Goyal, Ananya Kumar, Sankalp Garg, Zico Kolter, and Aditi Raghunathan. Finetune like you pre-train: Improved finetuning of zero-shot vision models. In *Proceedings of the IEEE/CVF Conference on Computer Vision and Pattern Recognition*, pages 19338–19347, 2023. 2

[15] Ibrahim Ethem Hamamci, Sezgin Er, Furkan Almas, Ayse Gulnihan Simsek, Sevval Nil Esirgun, Irem Dogan, Muhammed Furkan Dasdelen, Omer Faruk Durugol, Bastian Wittmann, Tamaz Amiranashvili, Enis Simsar, Mehmet Simsar, Emine Bensu Erdemir, Abdullah Alanbay, Anjany Sekuboyina, Berkcan Lafci, Christian Blauthgen, Mehmet Kemal Ozdemir, and Bjoern Menze. Developing Generalist Foundation Models from a Multimodal Dataset for 3D Computed Tomography, 2024. arXiv:2403.17834. 2, 3, 5, 7, 13, 14, 23

[16] Kaiming He, Xinlei Chen, Saining Xie, Yanghao Li, Piotr Dollár, and Ross Girshick. Masked autoencoders are scalable vision learners. In *Proceedings of the IEEE/CVF conference on computer vision and pattern recognition*, pages 16000–16009, 2022. 4

[17] Nicholas Heller, Fabian Isensee, Dasha Trofimova, Resha Tejpaul, Zhongchen Zhao, Huai Chen, Lisheng Wang, Alex Golts, Daniel Khapun, Daniel Shats, et al. The kits21 challenge: Automatic segmentation of kidneys, renal tumors, and renal cysts in corticomedullary-phase ct. *arXiv preprint arXiv:2307.01984*, 2023. 5

[18] Shih-Cheng Huang, Liyue Shen, Matthew P Lungren, and Serena Yeung. Gloria: A multimodal global-local representation learning framework for label-efficient medical image recognition. In *Proceedings of the IEEE/CVF international conference on computer vision*, pages 3942–3951, 2021. 2

[19] Shih-Cheng Huang, Zepeng Huo, Ethan Steinberg, Chia-Chun Chiang, Matthew P Lungren, Curtis P Langlotz, Serena Yeung, Nigam H Shah, and Jason A Fries. Inspect: a multimodal dataset for pulmonary embolism diagnosis and prognosis. In *Proceedings of the 37th International Conference on Neural Information Processing Systems*, pages 17742–17772, 2023. 13

[20] Fabian Isensee, Paul F Jaeger, Simon AA Kohl, Jens Petersen, and Klaus H Maier-Hein. nnu-net: a self-configuring method for deep learning-based biomedical image segmentation. *Nature methods*, 18(2):203–211, 2021. 5, 17, 24

[21] Fabian Isensee, Tassilo Wald, Constantin Ulrich, Michael Baumgartner, Saikat Roy, Klaus Maier-Hein, and Paul F Jaeger. nnu-net revisited: A call for rigorous validation in 3d medical image segmentation. In *International Conference on Medical Image Computing and Computer-Assisted Intervention*, pages 488–498. Springer, 2024. 5

[22] Gary H Kramer, Kevin Capello, Brock Bearrs, Aimée Lauzon, and Lysanne Normandeau. Linear dimensions and volumes of human lungs obtained from ct images. *Health physics*, 102(4):378–383, 2012. 17

[23] Ruochen Li, Jun Li, Bailiang Jian, Kun Yuan, and Youxiang Zhu. Reevalmed: Rethinking medical report evaluation by aligning metrics with real-world clinical judgment. *arXiv preprint arXiv:2510.00280*, 2025. 7

[24] Thomas J Littlejohns, Jo Holliday, Lorna M Gibson, Steve Garratt, Niels Oesingmann, Fidel Alfaro-Almagro, Jimmy D Bell, Chris Boultwood, Rory Collins, Megan C Conroy, et al. The uk biobank imaging enhancement of 100,000 participants: rationale, data collection, management and future directions. *Nature communications*, 11(1):2624, 2020. 13

[25] Haotian Liu, Chunyuan Li, Qingyang Wu, and Yong Jae Lee. Visual instruction tuning. *Advances in neural information processing systems*, 36:34892–34916, 2023. 5, 7, 24

[26] Ilya Loshchilov and Frank Hutter. Decoupled weight decay regularization. In *International Conference on Learning Representations*, 2019. 15

[27] Timo Lüddcke and Alexander Ecker. Image segmentation using text and image prompts. In *Proceedings of the IEEE/CVF conference on computer vision and pattern recognition*, pages 7086–7096, 2022. 2

[28] Kevis-Kokitsi Maninis, Kaifeng Chen, Soham Ghosh, Arjun Karpur, Koert Chen, Ye Xia, Bingyi Cao, Daniel Salz, Guangxing Han, Jan Dlabal, Dan Gnanapragasam, Mojtaba Seyedhosseini, Howard Zhou, and Andre Araujo. TIPS: Text-Image Pretraining with Spatial awareness, 2025. arXiv:2410.16512 [cs]. 2

[29] Asbjørn Munk, Jakob Ambsdorf, Sebastian Llambias, and Mads Nielsen. Amaes: Augmented masked autoencoder pretraining on public brain mri

data for 3d-native segmentation. *arXiv preprint arXiv:2408.00640*, 2024. 2, 19

[30] Muhammad Ferjad Naeem, Yongqin Xian, Xiaohua Zhai, Lukas Hoyer, Luc Van Gool, and Federico Tombari. Silc: Improving vision language pretraining with self-distillation. In *European Conference on Computer Vision*, pages 38–55. Springer, 2024. 2

[31] Maxime Oquab, Timothée Dariset, Théo Moutakanni, Huy V. Vo, Marc Szafraniec, Vasil Khalidov, Pierre Fernandez, Daniel HAZIZA, Francisco Massa, Alaaeldin El-Nouby, Mido Assran, Nicolas Ballas, Wojciech Galuba, Russell Howes, Po-Yao Huang, Shang-Wen Li, Ishan Misra, Michael Rabbat, Vasu Sharma, Gabriel Synnaeve, Hu Xu, Herve Jegou, Julien Mairal, Patrick Labatut, Armand Joulin, and Piotr Bojanowski. DINOv2: Learning robust visual features without supervision. *Transactions on Machine Learning Research*, 2024. Featured Certification. 4, 19, 23

[32] Suraj Pai, Ibrahim Hadzic, Dennis Bontempi, Keno Bressem, Benjamin H Kann, Andriy Fedorov, Raymond H Mak, and Hugo JW L Aerts. Vision foundation models for computed tomography. *arXiv preprint arXiv:2501.09001*, 2025. 5

[33] Suraj Pai, Ibrahim Hadzic, Dennis Bontempi, Keno Bressem, Benjamin H. Kann, Andriy Fedorov, Raymond H. Mak, and Hugo J. W. L. Aerts. Vision Foundation Models for Computed Tomography, 2025. 2

[34] Fernando Pérez-García, Rachel Sparks, and Sébastien Ourselin. TorchIO: a Python library for efficient loading, preprocessing, augmentation and patch-based sampling of medical images in deep learning. *Computer Methods and Programs in Biomedicine*, page 106236, 2021. 2, 13

[35] Fernando Pérez-García, Harshita Sharma, Sam Bond-Taylor, Kenza Bouzid, Valentina Salvatelli, Maximilian Ilse, Shruthi Bannur, Daniel C. Castro, Anton Schwaighofer, Matthew P. Lungren, Maria Teodora Wetscherek, Noel Codella, Stephanie L. Hyland, Javier Alvarez-Valle, and Ozan Oktay. Exploring scalable medical image encoders beyond text supervision. *Nature Machine Intelligence*, 2025. 24

[36] Alec Radford, Jong Wook Kim, Chris Hallacy, Aditya Ramesh, Gabriel Goh, Sandhini Agarwal, Girish Sastry, Amanda Askell, Pamela Mishkin, Jack Clark, et al. Learning transferable visual models from natural language supervision. In *International conference on machine learning*, pages 8748–8763. PMLR, 2021. 1, 2, 3, 15, 17

[37] Zhongyi Shui, Jianpeng Zhang, Weiwei Cao, Sinuo Wang, Ruizhe Guo, Le Lu, Lin Yang, Xianghua Ye, Tingbo Liang, Qi Zhang, and Ling Zhang. Large-scale and fine-grained vision-language pre-training for enhanced CT image understanding. In *The Thirteenth International Conference on Learning Representations*, 2025. 2, 5, 6, 20, 26

[38] Oriane Siméoni, Huy V Vo, Maximilian Seitzer, Federico Baldassarre, Maxime Oquab, Cijo Jose, Vasil Khalidov, Marc Szafraniec, Seungeun Yi, Michaël Ramamonjisoa, et al. DinoV3. *arXiv preprint arXiv:2508.10104*, 2025. 2, 4

[39] Amber L Simpson, Michela Antonelli, Spyridon Bakas, Michel Bilello, Keyvan Farahani, Bram Van Ginneken, Annette Kopp-Schneider, Bennett A Landman, Geert Litjens, Bjoern Menze, et al. A large annotated medical image dataset for the development and evaluation of segmentation algorithms. *arXiv preprint arXiv:1902.09063*, 2019. 5

[40] Yucheng Tang, Dong Yang, Wenqi Li, Holger R. Roth, Bennett Landman, Daguang Xu, Vishwesh Nath, and Ali Hatamizadeh. Self-supervised pre-training of swin transformers for 3d medical image analysis. In *Proceedings of the IEEE/CVF Conference on Computer Vision and Pattern Recognition (CVPR)*, pages 20730–20740, 2022. 2

[41] National Lung Screening Trial Research Team. The national lung screening trial: overview and study design. *Radiology*, 258(1):243–253, 2011. 4, 5, 13

[42] Qwen Team. Qwen2 technical report. *arXiv preprint arXiv:2407.10671*, 2024. 24

[43] Qwen Team. Qwen2.5 technical report. *arXiv preprint 2412.15115*, 2024. 5

[44] Michael Tschannen, Manoj Kumar, Andreas Steiner, Xiaohua Zhai, Neil Houlsby, and Lucas Beyer. Image captioners are scalable vision learners too. *Advances in Neural Information Processing Systems*, 36:46830–46855, 2023. 2, 4, 18

[45] Michael Tschannen, Alexey Gritsenko, Xiao Wang, Muhammad Ferjad Naeem, Ibrahim Alabdulmohsin, Nikhil Parthasarathy, Talfan Evans, Lucas Beyer, Ye Xia, Basil Mustafa, Olivier Hénaff, Jeremiah Harmen, Andreas Steiner, and Xiaohua Zhai. SigLIP 2: Multilingual Vision-Language Encoders with Improved Semantic Understanding, Localization, and Dense Features, 2025. arXiv:2502.14786 [cs]. 2, 17, 18, 19

[46] Maria De La Iglesia Vayá, Jose Manuel Saborit, Joaquim Angel Montell, Antonio Pertusa, Aurelia Bustos, Miguel Cazorla, Joaquin Galant, Xavier Barber, Domingo Orozco-Beltrán, Francisco García-García, et al. Bimcv covid-19+: A large annotated dataset of rx and ct images from covid-19 patients. *arXiv preprint arXiv:2006.01174*, 2020. 13

[47] Tassilo Wald, Saikat Roy, Fabian Isensee, Constantin Ulrich, Sebastian Ziegler, Dasha Trofimova, Raphael Stock, Michael Baumgartner, Gregor Köhler, and

Klaus Maier-Hein. Primus: Enforcing attention usage for 3d medical image segmentation. *arXiv preprint arXiv:2503.01835*, 2025. 3, 5, 15, 17, 19

[48] Tassilo Wald, Constantin Ulrich, Stanislav Lukyanenko, Andrei Goncharov, Alberto Paderno, Maximilian Miller, Leander Maerkisch, Paul Jaeger, and Klaus Maier-Hein. Revisiting mae pre-training for 3d medical image segmentation. In *Proceedings of the Computer Vision and Pattern Recognition Conference*, pages 5186–5196, 2025. 2, 19

[49] Tassilo Wald, Constantin Ulrich, Jonathan Suprijadi, Sebastian Ziegler, Michal Nohel, Robin Peretzke, Gregor Kohler, and Klaus Maier-Hein. An openmind for 3d medical vision self-supervised learning. In *Proceedings of the IEEE/CVF International Conference on Computer Vision*, pages 23839–23879, 2025. 2, 4, 5, 8, 13, 19, 24

[50] Bo Wan, Michael Tschannen, Yongqin Xian, Filip Pavetic, Ibrahim M Alabdulmohsin, Xiao Wang, André Susano Pinto, Andreas Steiner, Lucas Beyer, and Xiaohua Zhai. Locca: Visual pretraining with location-aware captioners. *Advances in Neural Information Processing Systems*, 37:116355–116387, 2024. 2, 18

[51] Zifeng Wang, Zhenbang Wu, Dinesh Agarwal, and Jiemeng Sun. Medclip: Contrastive learning from unpaired medical images and text. In *Proceedings of the Conference on Empirical Methods in Natural Language Processing. Conference on Empirical Methods in Natural Language Processing*, page 3876, 2022. 2

[52] Linshan Wu, Jiaxin Zhuang, and Hao Chen. Voco: A simple-yet-effective volume contrastive learning framework for 3d medical image analysis. In *Proceedings of the IEEE/CVF Conference on Computer Vision and Pattern Recognition (CVPR)*, pages 22873–22882, 2024. 2

[53] Tony Xu, Sepehr Hosseini, Chris Anderson, Anthony Rinaldi, Rahul G Krishnan, Anne L Martel, and Maged Goubran. A generalizable 3D framework and model for self-supervised learning in medical imaging. *NPJ Digit. Med.*, 8(1):639, 2025. 2

[54] An Yan, Julian McAuley, Xing Lu, Jiang Du, Eric Y Chang, Amilcare Gentili, and Chun-Nan Hsu. Radbert: adapting transformer-based language models to radiology. *Radiology: Artificial Intelligence*, 4(4):e210258, 2022. 5

[55] Xiaohua Zhai, Basil Mustafa, Alexander Kolesnikov, and Lucas Beyer. Sigmoid loss for language image pre-training. In *Proceedings of the IEEE/CVF International Conference on Computer Vision (ICCV)*, pages 11975–11986, 2023. 3

[56] Xiaohua Zhai, Basil Mustafa, Alexander Kolesnikov, and Lucas Beyer. Sigmoid Loss for Language Image Pre-Training. pages 11975–11986, 2023. 2, 17

[57] Yuhao Zhang, Hang Jiang, Yasuhide Miura, Christopher D Manning, and Curtis P Langlotz. Contrastive learning of medical visual representations from paired images and text. In *Machine learning for healthcare conference*, pages 2–25. PMLR, 2022. 3, 15

[58] Chong Zhou, Chen Change Loy, and Bo Dai. Extract Free Dense Labels from CLIP. In *Computer Vision – ECCV 2022*, pages 696–712, Cham, 2022. Springer Nature Switzerland. 2, 17

[59] Jinghao Zhou, Chen Wei, Huiyu Wang, Wei Shen, Ci-hang Xie, Alan Yuille, and Tao Kong. Image BERT pre-training with online tokenizer. In *International Conference on Learning Representations*, 2022. 2, 4

[60] Zongwei Zhou, Vatsal Sodha, Jiaxuan Pang, Michael B Gotway, and Jianming Liang. Models genesis. *Medical image analysis*, 67:101840, 2021. 2

A. Development framework

Due to the shortage of public 3D vision–language datasets such as CT-RATE [15], we believe the domain remains under-researched. We revisit key design decisions made by prior work to establish best practices for the 3D medical vision–language domain and iteratively ablate design decisions related to the adaptation of CLIP to 3D. Similarly, we ablate design decisions around the inclusion of radiology report generation and vision-only self-supervised learning. This is all conducted on chest CT, due to the availability of a large image-only dataset (NLST) and a large paired image–report dataset (CT-RATE).

A.1. Pre-training datasets

A.1.1 CT-RATE

The CT-RATE dataset [15] consists of 25 692 non-contrast CT acquisitions with associated reports from the Istanbul Medipol University Mega Hospital. Each report contains a *Findings* section, which describes the contents of the scan, and an *Impression* section, which represents an interpretation of the findings given the patient’s clinical history. The dataset is expanded to 50 188 unique 3D images by leveraging different reconstruction kernels for each acquisition. These kernels, or convolution algorithms, yield volumes with different spacings, with some reconstructions featuring high anisotropy, i.e., high in-plane resolution but low through-plane resolution, and others being less anisotropic. As the reconstructions stem from the same image acquisition, their information content is highly redundant. Therefore, for each acquisition, we choose the reconstruction with the lowest in-plane size to minimise computational cost. This yields a subset of 24 108 images, with a median spacing of $0.7 \times 0.7 \times 1.0$ mm and image size $512 \times 512 \times 359$ voxels (distribution of in-plane sizes: 22 417, 1648 and 43 images with size 512, 768, and 1024, respectively).

CT-RATE contains head CT scans, which we removed for all experiments and evaluations using the exclusion lists provided on the dataset repository. In total, our training split of CT-RATE is composed of 18 798 subjects with 22 676 unique 3D volumes, and the validation dataset holds 992 subjects with 1197 unique 3D volumes.

A.1.2 NLST

The National Lung Screening Trial (NLST) dataset [41] contains low-dose chest CT images from 26k patients, acquired at 33 different US centres, with each patient receiving one baseline scan and up to two follow-up scans at one-year intervals, yielding up to three scans per patient. Overall, this dataset provides about 72k chest CTs scans without associated reports, with two reconstruction kernels per acquisition. As both reconstructions have similar sizes, we

Table A.1. The scale of paired report-image 3D datasets is lower than the scale of large image-only 3D datasets. The number of acquisitions refers to unique scans, disregarding different CT reconstructions with multiple kernels.

Dataset	Body part and technique	Num. acquisitions
Paired images and reports		
BIMCV-R [46]	Chest CT	8k
INSPECT [19]	Chest CT pulmonary angiography (only <i>Impressions</i>)	23k
CT-RATE [15]	Chest CT	26k
Merlin [5]	Abdomen and pelvis CT	25k
Images only		
NLST [41]	Chest CT	72k
OpenMind [49]	Brain MRI	114k
Osteoarthritis Initiative (OAI)	Knee / thigh MRI	140k
UK Biobank [24]	Whole-body MRI	> 100k

randomly pick a reconstruction kernel for each acquisition, yielding our subset of NLST.

A.1.3 Other large datasets

Aside from the aforementioned CT-RATE and NLST, there are other large-scale paired image–report and large-scale image-only datasets in the domain, which we show in Tab. A.1 for additional context.

A.2. Image preprocessing

To conduct pre-training and classification experiments, we preprocessed CT-RATE, NLST and RAD-ChestCT to a unified format using TorchIO [34]. This preprocessing consisted of

1. Reorientation of all images to RAS+.
2. Dividing the CTs Hounsfield units by 1000, effectively mapping -1000 to -1 and +1000 to 1, respectively.
3. Clipping values outside of this range.
4. Resampling to 0.5-mm isotropic spacing, using an anti-aliasing Gaussian filter along any downsampled axes and B-Spline interpolation.

To perform efficient loading of 3D subvolumes from cloud storage during training, we stored the preprocessed images in the NIfTI-Zarr format, using `nifti-zarr-py` [2]. We also used `nifti-zarr-py` to generate versions of the each volume at 1-mm and 2-mm isotropic spacing, effectively storing a three-level Gaussian pyramid for each volume. The 1-mm- and 0.5-mm-spacing images were only used in conjunction with the vision-only pre-training paradigm.

A.3. Report preprocessing

CT-RATE contains image–report pairs, with each report containing *Findings* and *Impression* sections, as well as other sections we did not use. We processed the reports using GPT-4o (gpt-4o version 2024-08-06 through an Azure OpenAI endpoint) as explained below.

A.3.1 Translating from Turkish

The released reports in CT-RATE were originally translated from Turkish to English using the Google Translate API. We re-translated the reports to leverage the strong machine translation capabilities of modern large language models (LLMs), using the prompt in Sec. E.1.

A.3.2 Structuring into clinical subsections

We structured the *Findings* section by splitting it into clinical subsections, using the prompt in Sec. E.2:

1. *Image Quality*
2. *Lungs and Airways*
3. *Pleura*
4. *Mediastinum and Hila*
5. *Cardiovascular Structures*
6. *Bones and Soft Tissues*
7. *Tubes, Lines, and Devices*
8. *Upper Abdomen*.

Each sentence gets assigned in its original, long state to one of these subsections. Below is an example of the *Lungs and Airways* subsection:

The trachea and both main bronchi are patent, with no obstructive pathology detected. Ventilation of both lungs is normal, and no mass or infiltrative lesion is observed. Additionally, there is a hypodense lesion measuring 15 mm in diameter located in the posterolateral middle segment of the left lung, possibly a cyst.

These structured reports are used for the radiology report generation (RRG) objective.

A.3.3 Shortening individual findings

We split each subsection into short sentences representing *positive* and *negative* findings, using the prompt in Sec. E.3.

Each sentence is shortened and classified as a *positive* finding (i.e., mentions the presence of an abnormality) or as a *negative* finding (i.e., mentions normality). An example of the latter structure is shown in Fig. B.3 for the *Bones and Soft Tissues* subsection. The reports of this style are used for the *Short Sentence* augmentation and the Opposite Sentence Loss (OSL), which substantially improves our zero-shot classification metrics.

A.4. Global downstream tasks and datasets

To measure the quality and guide development of the trained vision and text encoder, we evaluate on global (as opposed to dense) tasks, specifically image-to-report retrieval, classification probes, and zero-shot classification. We use

CT-RATE to evaluate all of these tasks, as it includes image-report pairs (necessary for retrieval) as well as multi-abnormality labels for the 18 most common abnormalities in the dataset (necessary for zero-shot classification and the training of probes). To prevent data leakage between pre-training and downstream datasets, we divide the official CT-RATE training split into a train and a validation set. This split is identical to the split used in the original CT-CLIP paper (1k subjects with their associated reports and images) [15]. The official validation split of CT-RATE serves as our final test split.

During the development phase, we quantify retrieval performance through Recall at 1, 5, and 10 (R@1, R@5, R@10), and classification performance through *AUPRC* and *AUROC*, guiding the hyperparameter optimisation process. For a detailed explanation of the metrics, we refer to Sec. C.1.

For linear probing, we train five different sequence aggregation mechanisms with four different learning rates and a batch size of 16 for 15k steps with a cosine annealing learning rate schedule on the training split of CT-RATE. The best performing probe is selected based on its performance on our validation set of CT-RATE. This probe is later transferred for testing as-is to the test sets to yield the final predictions. More details on this are provided in Sec. C.2.

For zero-shot classification we differentiate between two zero-shot classification schemes.

1. **Native (N):** In ‘native’ zero-shot classification, we aggregate 50 reports of a patient with an abnormality and 50 reports of patients without this abnormality. Each of the long *Findings* is passed through the language encoder and the language pooler to yield 50 embeddings for positives and 50 embeddings for negatives. Each embeddings group is averaged to yield a representative embedding of the abnormality being present or absent from the reports.
2. **Short (S):** For each abnormality, a small template is used to create sentences about whether an abnormality is present or absent. We use ‘{abnormality} present’ and ‘no {abnormality} present’, respectively. The resulting embedding represents the presence or absence of this abnormality.

This differentiation allows us to disambiguate whether language encoders are able to handle both short-form and long-form text embeddings as inputs.

B. Extended methods and ablations

Translating the well-established contrastive language-image pre-training (CLIP) method from the 2D imaging domain to the 3D medical domain is difficult due to the large domain gap and has been explored less because of the previously mentioned lack of publicly available data. In this section, we start from the basic CLIP paradigm, ab-

lating multiple design choices, and iteratively extend the method with additional supervision objectives, yielding our Comprehensive Language–Image Pre-training (COLIPRI) encoder family (Fig. 2). The final hyperparameter configurations of this process are provided in Sec. B.5.

B.1. Adapting CLIP to 3D radiology

Due to the large domain differences between natural imaging and 3D medical imaging, crucial training settings can vary substantially, requiring re-tuning of hyperparameters traditionally used for 2D natural images. To narrow the overall optimisation search space, we fix a few hyperparameters. Namely, we choose to train a Primus-M vision transformer (ViT) encoder [47] with an AdamW [26] optimiser. Each model is trained for 250k or 125k steps with a total batch size of 8 or 16, respectively, resulting in 2 million training samples being seen by the model. We used 6.25k steps of linear learning rate warm-up, followed by a PolynomialLR schedule. We used a learning rate of 3×10^{-4} for batch size 8 and scaled linearly it with the batch size, when applicable. Aside from these fixed parameters, we chose an initial hyperparameter configuration that we optimise through a *star sweep* [1]. We chose a pre-trained CXR-BERT model [6] as the default text encoder due to the overlap of abnormalities between chest X-rays and chest CTs. By default, we pool dense vision and text tokens through a dedicated multi-head attention-pooling layer with 12 heads, trained from scratch for each encoder. We use the raw *Findings* section for supervision, and an input crop size of $192 \times 192 \times 192$ at 2-mm isotropic spacing. Pre-training experiments are conducted on Azure Machine Learning, using a single node with 4 A100 GPUs (80 GB VRAM), unless specified otherwise.

B.1.1 Report length

Tokenising radiology reports results in token sequences of substantial lengths, with the average *Findings* section of CT-RATE being 243 tokens long when using the tokeniser of CXR-BERT² (Fig. B.1). Consequently, training with long-form reports would inadvertently lead to a distribution shift when testing zero-shot classification with short-form prompts such as “{abnormality} present”. Moreover, medical zero-shot classification is typically performed through negated statements (“No {abnormality} present.”), which may be a problem due to such statements being very sparse during training.

To account for this, we introduce two ways of conducting zero-shot classification: ‘native’ and ‘short’ (Sec. A.4).

²This is in stark contrast to Zhang et al. [57] or Radford et al. [36], which use a maximum sequence length of 77 tokens. These works either sample a single sentence from the paired text or use datasets containing single-sentence captions.

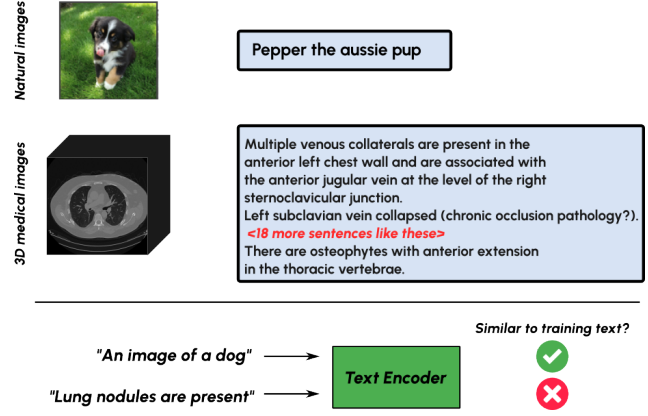


Figure B.1. **Reports of 3D medical images are substantially longer than captions of 2D natural images**, leading to a distribution shift between long reports seen during training and short prompts used for zero-shot classification if used naively. Additionally, long reports might allow the text encoder to overfit due to their high dimensionality, instead of learning semantics. We overcome these challenges with mechanisms such as the Opposite Sentence Loss (OSL) (Sec. B.4) and our pipeline for report pre-processing (Sec. A.3).

Table B.1. **Report augmentation ablations.** Long reports might cause the text encoder to overfit, which we mitigate by introducing *Sentence Shuffle* (here, ‘Shuffle’) and *Short Sentence* (here, ‘Shorten’) augmentations.

	Retrieval			Probing		Zero-shot (N)		Zero-shot (S)	
	R@1	R@5	R@10	AUPRC	AUROC	AUPRC	AUROC	AUPRC	AUROC
Default	8.27	22.64	31.66	55.41	83.11	43.48	76.48	34.77	66.91
Shuffle	11.11	28.57	37.93	56.66	83.94	44.05	76.55	35.13	69.21
Shorten									
$p = 0.10$	12.71	29.01	39.30	56.91	83.76	45.81	77.93	39.55	71.15
$p = 0.25$	11.54	27.68	38.04	56.45	83.87	47.12	78.67	35.13	68.10
$p = 0.50$	11.20	28.01	38.21	56.32	83.91	46.07	78.63	37.09	70.24
$p = 0.75$	9.78	25.92	34.36	56.97	84.01	46.41	78.74	34.70	68.19

The overall shift between these two zero-shot prompting schemes is presented in Tab. B.1, showing a 10-pp AUROC and AUPRC gap between them for our default CLIP configuration. The difference in performance between evaluation styles reveals that zero-shot classification in medical vision–language encoders (VLEs) may be highly sensitive to linguistic formulation, with short diagnostic phrases (often not seen during training) yielding weaker alignment than native report-style embeddings.

To minimise the distribution shift and reduce overfitting to the structure of long text reports, we introduce a *Sentence Shuffle* transform, which randomly shuffles sentences in the reports, substantially improving both retrieval and classification performance (Fig. B.2). Additionally, we introduce a *Short Sentence* augmentation that replaces long-form reports with a shortened version. These shortened reports were created using GPT-4o with instructions to reduce verbosity to a minimum (Sec. A.3 and Fig. B.3). Combin-

Table B.2. **Ablations related to the text used for training our COLIPRI models.** *Impressions*: Training with impressions instead of findings; *Findings + Impressions*: Training with findings and impressions concatenated; *Re-translated*: Using GPT-4o to re-translate the reports from Turkish to English; *Shuffle*: Using the *Sentence Shuffle* augmentation; *DnC*: Did not Converge;

	Retrieval			Probing		Zero-shot (N)		Zero-shot (S)	
	R1	R5	R10	AUPRC	AUROC	AUPRC	AUROC	AUPRC	AUROC
Default	8.27	22.64	31.66	55.41	83.11	43.48	76.48	34.77	66.91
Sentence Shuffle	11.11	28.57	37.93	56.66	83.94	44.05	76.55	35.13	69.21
Findings	8.27	22.64	31.66	55.41	83.11	43.48	76.48	34.77	66.91
Impressions	7.77	21.80	30.58	54.89	83.29	43.74	76.52	29.11	62.40
Findings + Impressions	8.69	22.22	31.83	55.31	83.27	43.64	76.74	31.39	67.64
Original translation	8.27	22.64	31.66	55.41	83.11	43.48	76.48	34.77	66.91
Re-translate	7.53	20.90	29.35	55.24	83.00	42.69	76.29	28.29	60.11
Re-translate + Shuffle	9.95	24.58	32.27	56.21	83.64	44.22	76.73	32.05	67.19
BiomedCLIP	3.43	13.28	19.47	52.79	81.89	37.43	74.21	28.16	59.30
CXR-BERT (scratch)	DnC	DnC	DnC	DnC	DnC	DnC	DnC	DnC	DnC
CXR-BERT (pre-trained)	8.27	22.64	31.66	55.41	83.11	43.48	76.48	34.77	66.91

Multiple venous collaterals are present in the anterior left chest wall and are associated with the anterior jugular vein at the level of the right sternoclavicular junction.
Left subclavian vein collapsed (chronic occlusion pathology?).
<other sentences>
There are osteophytes with anterior extension in the thoracic vertebrae.

Random permutation

Subsegmental atelectasis is observed in the right middle lobe.
<other sentences>
Left subclavian vein collapsed (chronic occlusion pathology?).
There are osteophytes with anterior extension in the thoracic vertebrae.
When examined in the lung parenchyma window:
Linear atelectasis is present in both lung parenchyma.
The left kidney partially entering the section is atrophic.

Figure B.2. **Sentence shuffling regularises the order of sentences**, removing potential ordering biases of practitioners when writing their reports. Sentences are split using periods “.” as delimiter.

ing *Sentence Shuffle* with the *Short Sentence* augmentations yielded further improvements in retrieval and classification (Tab. B.1). In particular, the addition of the *Short Sentence* transform increases our short zero-shot classification performance considerably, reducing the gap between our ‘native’ and ‘short’ zero-shot classification settings (Sec. A.4).

Aside from investigating text augmentations, we evaluate the influence of training with *Impressions* or *Findings + Impressions*, as well as training with a translation of the original Turkish reports to English using modern methods that might reflect clinical terminology more accurately. Results are visualised in Tab. B.2, highlighting that *Findings + Impressions* is better than only *Impressions*; however, using only the *Findings* is superior to both. The results also show that the newer translation does not positively affect performance, hence we do not use the original translation for the report-to-image alignment objective³.

Our default text encoder is CXR-BERT, a transformer

³Our translations were still used to create the clinical subsections.

Multiple venous collaterals are present in the anterior left chest wall and are associated with the anterior jugular vein at the level of the right sternoclavicular junction.
Left subclavian vein collapsed (chronic occlusion pathology?).
<other sentences>
There are osteophytes with anterior extension in the thoracic vertebrae.

Structuring, shortening, categorization through GPT endpoint

Resulting Report in JSON format

```
{
  "bones_and_soft_tissues": [
    "negative_findings": [],
    "positive_findings": [
      "Osteophytes on thoracic vertebrae."
    ],
    ...
  ]
}
```

Concatenate in random order

Collapsed left subclavian vein.
Minimal peribronchial consolidation.
Osteophytes on thoracic vertebrae.
<other sentences>
Airway wall thickening with tree-in-bud pattern.
No lymph node enlargement.
Pleura unremarkable.
Venous collaterals in anterior left chest.

Figure B.3. **Reports structuring and sentence shortening** reduce the domain shift between long reports seen during training time and short texts used for zero-shot classification.

pre-trained on chest X-ray reports that we fine-tune. Since this model is relatively small, holding about 110M parameters, and was trained on substantially shorter X-ray reports, we also evaluated the effect of using a larger text encoder. We tested the 196M-parameter BiomedCLIP model, which was pre-trained on the entire PubMed collection (15 million biomedical image–text pairs), as well as training our CXR-BERT architecture from scratch. Results are presented in Tab. B.2 at the bottom, showing the superiority of CXR-BERT over the larger BiomedCLIP model.

B.1.2 Field of view and number of patches

Radiological reports typically describe findings across the entire field of view (FOV), rather than a restricted subregion. For example, chest CT reports primarily focus on pulmonary disease but often also include findings about visible abdominal organs and other incidental findings.

In chest CT classification, the relevant abnormalities may be localised in specific lobes or distributed across the lungs. Therefore, the model must have access to the en-

tire lungs FOV to avoid missing critical context. Training only on sub-crops may act as a form of regularisation, but, at inference time, such models may not classify images reliably without a global FOV since important abnormalities might lie outside the cropped region. Practically, this requires very large input volumes for training. At a resolution of 2 mm isotropic spacing, an input size of $192 \times 192 \times 192$ voxels corresponds to a cube with edge 38.4 cm. This FOV should suffice to cover the lungs, which are typically under 30 cm across all anatomical axes [22]. However, when using a patch size of $8 \times 8 \times 8$ voxels in the ViT (the default in Primus, as larger patches often degrade performance on high-resolution dense downstream tasks [47]), the number of patches in a sequence reaches 14k tokens. This is orders of magnitude longer than typical vision-language settings, where natural images tokenised at standard patch sizes yield only $(224/14)^2 = 256$ tokens [45]. This raises two fundamental questions: i) Are large FOVs required for good performance? ii) How does one best aggregate this long token sequence into a global representation? To address these issues, we evaluate the effects of varying input size, token patch size, and token aggregation strategy, as well as removing absolute positional encodings (APEs) to allow varying the input size at test time (Tab. B.3).

Our results indicate that smaller input sizes are beneficial, while larger inputs reduce overall performance (Tab. B.3 - *Input Size*). The only exception to this is the ‘short’ zero-shot classification, where an input size of $128 \times 128 \times 128$ performs worst. Why hypothesise that smaller input sizes improve performance by forcing the vision encoder to learn more robust and semantically meaningful representations. Larger FOVs expose all abnormalities simultaneously, allowing the encoder to rely on only a subset of correlated features. In contrast, smaller crops limit the visible context, incentivising the model to capture multiple discriminative cues. While this suggests that small input sizes as small as 128 may be better, an excessively small input size will discard a large amount of relevant information, limiting the applicability of the model. Additionally, we observe that reducing the sequence length through the use of a larger patch size has detrimental effects on overall performance (Tab. B.3 - *Patch size*), forcing us to keep the fine-grained tokens and rather long resulting sequences at the cost of higher computational resources. Aggregating this sequence through max-pooling proved to be the best mechanism for retrieval and linear probing. However, our default multi-head attention pooling proved superior for zero-shot classification and yields competitive results across all metrics (Tab. B.3 - *Token aggregation method*), while allowing one to use the MaskCLIP trick [58] to generate language-aligned dense embeddings for segmentation. Lastly, we find that removing the APE only negatively affects *short* zero-shot classification, which we found to be the noisiest metric

Table B.3. Field of view and patch size ablations. Smaller patch sizes are better, while using a large field of view is less relevant. To yield global representations, max-pooling performs very well for retrieval, while multi-head attention pooling performs well across the board.

Patch size	Retrieval			Probing		Zero-shot (N)		Zero-shot (S)	
	R@1	R@5	R@10	AUPRC	AUROC	AUPRC	AUROC	AUPRC	AUROC
$16 \times 16 \times 16$	5.76	14.62	22.14	49.88	81.05	40.71	75.12	29.58	61.80
$8 \times 8 \times 8$	8.27	22.64	31.66	55.41	83.11	43.48	76.48	34.77	66.91
Input size									
$128 \times 128 \times 128$	8.35	22.06	29.66	56.19	83.78	44.60	77.17	32.00	63.05
$160 \times 160 \times 160$	7.94	23.64	32.75	55.91	83.51	43.22	76.24	34.77	66.70
$192 \times 192 \times 192$	8.27	22.64	31.66	55.41	83.11	43.48	76.48	34.77	66.91
$224 \times 224 \times 224$	-	-	-	54.44	83.06	42.69	76.13	29.99	64.78
No absolute positional encoding	9.27	23.48	33.33	55.38	83.20	43.30	76.18	25.07	58.56
Token aggregation method									
Avg. pooling	5.93	18.88	27.90	54.34	83.03	40.20	75.48	35.65	67.46
Max pooling	11.45	27.57	38.01	56.18	83.56	42.80	75.32	25.86	56.57
Single-head attention pooling	5.43	19.13	27.57	54.05	82.82	40.84	75.83	33.27	62.19
Multi-head attention pooling	8.27	22.64	31.66	55.41	83.11	43.48	76.48	34.77	66.91

Table B.4. Other ablations. An optimal trade-off is achieved by balancing batch size with reduced training iterations. The sigmoid loss formulation does not improve performance. Lastly, minor spatial augmentations and low levels of intensity augmentation or not using intensity augmentations at all are best.

Batch size - training Steps	Retrieval			Probing		Zero-shot (N)		Zero-shot (S)	
	R@1	R@5	R@10	AUPRC	AUROC	AUPRC	AUROC	AUPRC	AUROC
8 - 250k	8.27	22.64	31.66	55.41	83.11	43.48	76.48	34.77	66.91
16 - 125k	9.77	24.98	32.75	55.66	83.44	41.68	75.48	31.82	63.40
24 - 62.5k	8.10	23.89	31.75	55.95	83.51	43.13	76.05	30.87	62.27
32 - 31.7k	8.27	20.05	29.32	55.19	83.23	40.55	74.77	23.69	53.89
Loss type									
Softmax loss	8.27	22.64	31.66	55.41	83.11	43.48	76.48	34.77	66.91
Sigmoid loss	5.60	16.21	24.06	53.88	82.81	39.45	74.66	30.90	63.44
Image augmentation (spatial - intensity)									
low - off	8.27	22.64	31.66	55.41	83.11	43.48	76.48	34.77	66.91
low - low	9.02	22.47	30.49	55.73	83.65	43.43	76.05	31.90	63.28
high - high	4.59	15.96	23.73	54.91	83.11	41.44	76.16	30.71	59.63

during our development. Hence, we chose to accept these minor penalties as a trade-off to allow dynamically adapting the input size (Tab. B.3 - *No absolute positional encoding*).

B.1.3 Other ablations

Contrastive learning in natural imaging benefits from large batch sizes, with e.g. 32k in Tschannen et al. [45]. This is far out of reach for 3D medical imaging, where batch sizes are, e.g., two when training segmentation models with nnU-Net [20], due to high VRAM consumption. Subsequently, we ablate the trade-off between larger batch sizes versus fewer iterations, while keeping the amount of seen samples identical. Lastly, we evaluate whether a sigmoid loss [56] improves performance compared to the default softmax loss [36], and determine the extent to which strong spatial and intensity augmentations are necessary. Results are provided in Tab. B.4. We find mid-sized batches with fewer iterations to be superior and a decrease in performance when using the sigmoid loss. We also find low levels of intensity and spatial augmentations optimal, with stronger augmentations degrading performance.

B.1.4 Merging all changes

Based on our previous ablations, we introduce changes to our `default` configuration. We i) increase the batch size to 16, in conjunction with doubling our learning rate to 6×10^{-4} and halving our iterations to 125k, ii) reduce the input size to $160 \times 160 \times 160$, iii) add the *Sentence Shuffle* and *Short Sentence* text augmentation using LLMs, iv) add image intensity augmentations, v) remove the APE as it is not necessary, which also allows varying the input size of the model at inference time. The final hyperparameters chosen from the prior ablations are presented in Tab. B.8, which, together with the OSL, yield our `COLIPRI-C` encoder.

B.2. Including text generation

The goal of CLIP is to align image-report pairs. This objective can be a limiting factor in the medical domain, since there may exist multiple features that differentiate two image-report pairs, but a single one can suffice to distinguish them. This key insight spurred recent works to introduce the objective of predicting the image caption from the embedding of the image encoder [44, 45, 50]. To solve this task, the vision embeddings need to contain information about everything mentioned in the text report, as opposed to only about what differentiates two image-report pairs. Additionally, this objective is independent of the batch size, which is particularly important for a batch-size-constrained domain like 3D medical imaging. In this work, we combine the CLIP objective with a radiology report generation (RRG) objective based on CapPa [44], which conducts either *causal captioning* or *parallel captioning* in an interleaved fashion, i.e., alternating at each training iteration, to generate a report during training. *Causal captioning* refers to predicting the report in a next-word-prediction fashion using causal masking, while *parallel captioning* predicts the entire report simultaneously from a fully masked input.

B.2.1 Radiology report generation for vision pre-training

As mentioned in Sec. B.1.1, medical reports and natural image captions differ significantly, with medical reports being substantially longer and presenting a structure more akin to a list. These aspects can pose hurdles in RRG, as the ordering of a listing is unpredictable without learning the preferences of the clinician who wrote the report or without memorising the entire report, both of which are undesirable. To address this, we structure the reports by assigning each sentence to one of eight semantic categories (Sec. A.3). Given these structured reports, we train our text decoder to generate the reports in a causal and a parallel fashion, but leave the clinical subsection headers unmasked to guide the generation. This suffices for the *captioning*; however, for *parallel captioning*, we expect the amount of masked tokens

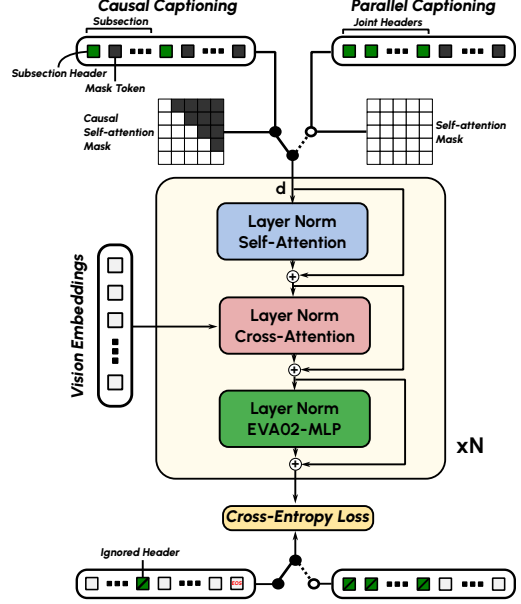


Figure B.4. **Text generation pre-training.** To yield more semantic image features, we feed them through cross-attention into our text decoder EVA-02 transformer architecture, tasked with *causal captioning* or *parallel captioning*. This is optimised simultaneously with the CLIP objective.

between two subsection headers to leak information as no causal attention mask is used. This is due to subsections being longer when pathological findings are present, which would allow the generative decoder to infer whether abnormalities are present given the number of masked tokens in the subsection. To remove this bias, we group the headers at the start of the report, followed by mask tokens. This informs the decoder of the desired ordering of the subsections, without leaking the length of each subsection. For both of our generative tasks, we shuffle the order of the subsections during training to regularise the decoder. Given this task formulation, we followed Tschannen et al. [44] and used a cross-attention-based approach to integrate vision tokens with a small transformer decoder. The causal and parallel text decoding setting is visualised in Fig. B.4.

B.2.2 Report generation optimisations

When combining the optimised CLIP configuration with the RRG objective, there are a few design decisions that warrant optimisation. By default, we choose a generator depth of 12 layers, a 50/50% probability of causal versus parallel captioning, and a loss weight of $\lambda_{RRG} = 1$, with $\mathcal{L}_{total} = \mathcal{L}_{CLIP} + \lambda_{RRG} \cdot \mathcal{L}_{RRG}$. For these parameters, we conduct another star sweep [1] from our `default` configuration (Tab. B.5). Our results indicate that always using the *parallel captioning* loss is better than including also the *causal*

Table B.5. RRG objective optimisations. Shorter generator depth, lower RRG loss weight, and only using parallel captioning improve performance. Relative to the COLIPRI-C model, the inclusion of the RRG objective increases retrieval performance while reducing the classification performance.

	Retrieval			Probing		Zero-shot (N)		Zero-shot (S)	
	R@1	R@5	R@10	AUPRC	AUROC	AUPRC	AUROC	AUPRC	AUROC
Depth of text decoder									
4	9.52	25.31	33.25	55.85	83.40	46.29	76.53	37.69	69.41
6	11.70	26.57	35.42	55.72	83.28	44.73	75.88	34.56	69.39
8	10.44	24.56	32.41	54.14	82.59	45.20	75.80	31.23	60.90
12	10.03	24.06	32.33	55.09	82.89	43.87	75.35	32.94	66.49
CapPa-Cap Probability (%)									
0-100	8.10	22.72	30.33	54.53	82.80	44.66	74.97	35.11	63.22
25-75	9.44	21.81	29.24	54.27	73.52	43.48	75.59	29.28	61.28
50-50	10.03	24.06	32.33	55.09	82.89	43.87	75.35	32.94	66.49
75-25	10.36	25.31	34.34	55.32	83.28	45.80	77.03	35.82	68.63
100-0	11.03	24.65	34.25	56.36	83.42	44.89	75.64	31.13	61.41
λ_{RRG}									
0.1	11.03	26.15	35.09	55.79	83.14	45.56	76.43	33.65	64.59
0.3	9.27	24.48	33.00	55.29	83.17	45.38	76.70	36.46	68.09
1	10.03	24.06	32.33	55.09	82.89	43.87	75.35	32.94	66.49

captioning objective. This is likely due to the next-word (*causal captioning*) objective learning to memorise long reports, resulting in the vision tokens not being required for the decoding. Moreover, we observed that lower decoder depths are more beneficial than deeper decoders, forcing vision embeddings to be quickly adoptable for report generation. Lastly, we observe an intermediate loss weight of 0.3 to be optimal and found it necessary to decrease the learning rate to 3×10^{-5} due to training instability. Combining these changes together with the Opposite Sentence Loss (OSL) yields the COLIPRI-CR encoder.

Interestingly, we observe that the additional generative decoding objective increases retrieval performance. However, it improves classification probing and zero-shot classification just slightly. Interestingly, this objective did not improve our RRG results. This indicates that the current generative decoding objective may still be subject to confounders that prevent the vision encoder from learning semantically meaningful representations, which would further increase linear separation of abnormalities.

B.3. Including vision-only self-supervision

While vision–language pre-trained encoders tend to learn useful representations for global reasoning tasks, they require paired data and their learnt representations are often less powerful for dense tasks [31], which represent the majority of the challenges in the medical imaging community [47]. To improve the quality of the learnt embeddings of our vision encoder for dense tasks, we pair our vision–language pre-training with an additional masked image modelling (MIM), vision-only objective, yielding COLIPRI-CM.

Given the recent OpenMind benchmark [49], we choose MAE as our vision-only objective, mostly due to the lack of more advanced dense pre-training methods such as iBOT,

Table B.6. MAE optimisations. Increasing the masked autoencoder (MAE) depth to 6, using block masking, and including the MAE loss only for the last 25% of training improves performance. Other changes were deemed not relevant.

	Retrieval			Probing		Zero-shot (N)		Zero-shot (S)	
	R@1	R@5	R@10	AUPRC	AUROC	AUPRC	AUROC	AUPRC	AUROC
MAE decoder depth									
2	14.04	30.91	39.77	55.15	82.95	44.61	76.31	38.15	70.84
4	13.28	30.41	38.60	54.81	83.13	44.22	76.76	40.55	73.70
6	14.45	33.42	41.52	55.71	83.44	45.22	77.04	38.14	71.50
8	12.78	29.99	39.68	55.04	82.95	44.73	76.81	37.30	70.70
Masking ratio									
60%	13.78	30.83	38.85	55.08	83.17	44.71	76.14	38.76	72.57
75%	13.28	30.41	38.60	54.81	83.13	44.22	76.76	40.55	73.70
90%	14.20	32.08	41.85	55.41	83.02	44.32	76.32	37.92	71.94
Mask style									
Random	13.28	30.41	38.60	54.81	83.13	44.22	76.76	40.55	73.70
Block	14.87	29.74	38.68	55.46	83.12	44.63	76.84	39.33	72.45
Inverse block	13.37	30.41	40.02	55.44	83.19	45.01	76.83	39.22	72.37
Included at last X% of training									
25%	13.95	29.07	36.51	56.41	83.83	45.42	76.57	41.99	74.95
50%	12.95	29.91	38.68	56.40	83.39	45.26	76.63	40.65	72.83
75%	14.54	30.08	38.35	56.62	83.28	45.64	77.47	36.92	70.81
100%	13.28	30.41	38.60	54.81	83.13	44.22	76.76	40.55	73.70
λ_{MAE}									
0.1	14.62	29.16	37.59	54.99	83.07	44.82	76.57	32.75	66.17
0.5	13.62	29.91	38.68	55.34	83.06	44.77	76.49	40.10	72.25
1.0	13.28	30.41	38.60	54.81	83.13	44.22	76.76	40.55	73.70
2.0	14.62	31.75	40.52	55.08	83.07	45.05	76.96	37.31	69.74
Smallest isotropic spacing included									
2 mm	13.28	30.41	38.60	54.81	83.13	44.22	76.76	40.55	73.70
1 mm	15.46	31.66	39.77	56.19	83.44	43.16	76.48	41.35	74.90
0.5 mm	14.29	29.57	38.60	55.19	82.98	43.38	76.12	40.67	73.51

DINOv2, and DINOv3 in 3D medical imaging. To simplify integration of the vision-only objective and to save time by ablating COLIPRI-CR and COLIPRI-CM in parallel, we also integrate the MAE pre-training with our COLIPRI-C encoder and then combine the optimised configurations of COLIPRI-CR and COLIPRI-CM to yield COLIPRI-CRM.

MAE objectives are prevalent in the domain and often subject to high masking ratios of 60 to 90% [29, 48]. These high masking ratios occlude most of the image, which we expect to hinder the CLIP task. To minimise this interference, we alternate between vision-only and vision–language objectives for each training batch, following Tschannen et al. [45].

As the vision-only objective is not subject to the large FOV problem (Sec. B.1.2), we can expose our models to sub-crops at higher resolutions and incorporate the image-only NLST dataset into our training data.

B.3.1 Vision-only optimisations

Analogous to RRG, the inclusion of the MAE objective introduces several factors of variation deserving ablation. In particular, we ablate the masking ratio, masking style (random, block and inverse block masks), mask decoder depth, vision-only loss weight λ_{MAE} , as well as ablating whether later inclusion of the vision-only objective is beneficial [45]. We also assess the inclusion of higher-resolution images, evaluating the effect of including images resampled to 1-mm and 0.5-mm isotropic spacings. Results are visualised

in Tab. B.6.

Despite slight performance decreases in retrieval and classification, we chose to always include the vision-only objective in the training of the vision–language model to improve the segmentation performance. Moreover, initialising the vision-encoder with MAE pre-trained weights showed to reduce the negative effect of the MAE objective on global tasks and improved segmentation performance substantially (Tab. D.5).

We find the masking ratio of 75% to be optimal in combination with random masking, as well as using a vision-only loss weight of 1. We encountered training stability issues when training with the same learning rate, so it was reduced by a factor of 2 to 3×10^{-5} . Lastly, we chose to only include images of 2-mm isotropic and 1-mm isotropic spacing, finding no benefit in including images with 0.5-mm isotropic spacing. The final hyperparameters are presented in Tab. B.10.

B.4. The Opposite Sentence Loss

The Opposite Sentence Loss (OSL) is designed to address a core limitation of vision–language pre-training in the medical domain: the linguistic distribution shift between the verbose reports seen during training and the concise diagnostic prompts used at inference time. While radiology reports describe multiple organs and findings, often using long-form sentences with redundant context, clinical inference and zero-shot evaluation are typically conducted through short, polarity-sensitive queries such as “Lung nodules” or “No lung nodules”. This mismatch can degrade performance because the text encoder learns to align volumetric image features with long-form report embeddings rather than compact, semantically precise statements.

B.4.1 Motivation and intuition

The OSL explicitly trains the model to differentiate between semantically opposing statements that differ only in their diagnostic polarity. It encourages the joint embedding space to encode the distinction between the presence and absence of findings, improving the zero-shot classification task. By introducing pairs of positive and negated sentences, the OSL exposes the text encoder to the same short, diagnostic phrases used at inference in an open-set fashion, narrowing the training–inference gap.

B.4.2 Related works

In Merlin [5], every other step of model training is performed with sentences that mention only one organ. Sentences not about this particular organ are removed, reducing sentence length. In fVLM [37], sentences are also assigned to particular organs, aligning the text embeddings only with the image tokens corresponding to the particular

organ. Both of these approaches reduce the shift between training and zero-shot classification.

Contrary to the aforementioned methods, our proposed OSL does not require to pair sentences with a localised structure (e.g., the liver). Our OSL removes the need for any explicit spatial priors. Consequently, it can learn semantically meaningful embeddings for short sentences even when they are not spatially grounded to a particular anatomical structure. Instead, it just requires the practitioner to think of any categorisation of sentences *without requiring those categories to be localisable*.

B.4.3 Pair construction

Let \mathcal{R} be all LLM-preprocessed reports described in Sec. A.3 (see Fig. E.1 for an example), and let (x_i, r_i) be a random image-report pair with $r_i \in \mathcal{R}$. Each report r_i is composed of eight clinical subsections \mathcal{C} , with each clinical subsection $c_i = c_i^+ \cup c_i^-$ being composed of *positive findings* and *negative findings*, with $c_i^+ = \{s_1^+, \dots, s_j^+\}$ holding $j \geq 0$ *positive finding* sentences s^+ . Given all positives sentences in r_i

$$S_i^+ = \bigcup_{c \in \mathcal{C}} c_i^+ \quad (1)$$

we uniformly sample a positive sentence $s_i^+ \sim S_i^+$. We create a negation of s_i^+ via a simple negation template:

$$s_i^- = \text{“No } \{\text{sentence}\}” \quad (2)$$

This yields a semantically opposing pair (s_i^+, s_i^-) that differ only in diagnostic polarity.

To ensure that opposing sentence pairs are not generated solely from subsections containing true findings in r_i , we additionally identify all clinical subsections C_{zero} such that all $c_i^+ \in C_{zero}$ have no positive findings: $|c_i^+| = 0$. Given $c \in C_{zero}$ we sample random positive findings from these subsections from all reports

$$s_i^+ \sim \bigcup_{k \in \mathcal{R}} \bigcup_{c \in C_{zero}} c_k^+. \quad (3)$$

As before, we create a negation s_i^- with the template, yielding another pair (s_i^+, s_i^-) . Since this s_i^+ is a *positive finding* that does *not* originate from r_i , it does not provide a correct description of the image content, making its negation s^- a correct statement.

Thus, we define the binary supervision label $y_i \in \{0, 1\}$ according to whether the positive statement s_i^+ is supported by the current image:

$$y_i = \begin{cases} 1, & \text{if } s_i^+ \in r_i, \\ 0, & \text{otherwise.} \end{cases} \quad (4)$$

As such, if a positive finding originates directly from the current report, s_i^+ corresponds to the true observation

Algorithm 1: Opposed Sentence Transform (OST)

Input: Structured report r_i for image x_i ; database of positive findings S_{db}^+ grouped by subsection; number of sentence pairs K ; negation function $\text{Negate}(\cdot)$

Output: Sentence list T_i of length $2K$ and label list Y_i of length K

$$T_i \leftarrow [] ; Y_i \leftarrow []$$

$$S_i^+ \leftarrow \text{all positive findings in } r_i$$

$$C_{\text{zero}} \leftarrow \text{subsections of } r_i \text{ with no positive findings}$$

$$P_{\text{true}} \leftarrow \text{sample } \min(K, |S_i^+|) \text{ sentences from } S_i^+$$

$$P_{\text{fake_pool}} \leftarrow \emptyset \quad // \text{ Set to deduplicate}$$

for each subsection $c \in C_{\text{zero}}$ do

$$P_{\text{fake_pool}} \leftarrow P_{\text{fake_pool}} \cup \text{positive findings from } S_{\text{db}}^+[c]$$

$P_{\text{false}} \leftarrow \text{sample } \min(K, |P_{\text{fake_pool}}|) \text{ sentences from } P_{\text{fake_pool}}$

$n_{\text{true}} \leftarrow \min(\lceil K/2 \rceil, |P_{\text{true}}|)$

$n_{\text{false}} \leftarrow \min(\lfloor K/2 \rfloor, |P_{\text{false}}|)$

$P_{\text{true}} \leftarrow \text{sample } n_{\text{true}} \text{ from } P_{\text{true}}$

$P_{\text{false}} \leftarrow \text{sample } n_{\text{false}} \text{ from } P_{\text{false}}$

for each $s^+ \in P_{\text{true}}$ do

$$T_i.\text{append}(s^+)$$

$$T_i.\text{append}(\text{Negate}(s^+))$$

$$Y_i.\text{append}(1)$$

for each $s^+ \in P_{\text{false}}$ do

$$T_i.\text{append}(s^+)$$

$$T_i.\text{append}(\text{Negate}(s^+))$$

$$Y_i.\text{append}(0)$$

// Padding to fixed length

while $|Y_i| < K$ **do**

$$T_i.\text{append}(""); T_i.\text{append}("")$$

$$Y_i.\text{append}(-1) \quad // \text{ ignored in loss}$$

return T_i, Y_i

in the image, and the correct (ground-truth) label is therefore $y_i = 1$, otherwise $y_i = 0$. This ensures that both true and counterfactual examples (s_i^+, s_i^-) are presented to the model, encouraging robust discrimination from clinically valid versus invalid findings. Pseudocode for this *Opposed Sentence Transform (OST)* algorithm is provided in Algorithm 1.

B.4.4 Loss formulation

Let v_i denote the global image embedding for case i , and let s_i^+ and s_i^- represent the positive and negated plain-text sentences. If s_i^+ originates from the report of case i , the sentence correctly describes the image, yielding label $y_i = 1$. Should s_i^+ originate from another report, the state-

ment would not apply to the image, as no positive findings have been reported for this image, hence the label of the sentence pair would be $y_i = 0$. Using our text encoder, we create embeddings for both sentences, yielding embedding e_i^+ and e_i^- for the corresponding positive and negated sentence embeddings, respectively. For each pair (e_i^+, e_i^-) , we compute cosine similarity scores between the image and both sentence embeddings. After applying a temperature scaling factor τ , we convert the two similarities into probabilities using a softmax function:

$$p_i^+ = \frac{\exp(\text{sim}(v_i, e_i^+)/\tau)}{\exp(\text{sim}(v_i, e_i^+)/\tau) + \exp(\text{sim}(v_i, e_i^-)/\tau)} \quad (5)$$

The OSL objective is then a binary cross-entropy loss encouraging the true embeddings to be more similar to the image embedding than the false embedding:

$$\mathcal{L}_{\text{OSL}} = -\frac{1}{N} \sum_{i=1}^N \left[y_i \log p_i^+ + (1 - y_i) \log(1 - p_i^+) \right] \quad (6)$$

where N is the batch size.

Due to the larger sequence length of our image tokens, doing an image forward pass is expensive. As the text sequence is two orders of magnitude shorter, we create eight positive and negative sentence pairs (16 sentences total) for each image, for an efficient forward pass. The formalisation above does not include the index for the multiple sentences per image-report pair for clarity in this paragraph.

B.4.5 Integration with CLIP

During multimodal training, the OSL operates alongside the standard CLIP contrastive loss. Both losses act on the same image-text pairs but at different levels of semantic granularity: CLIP aligns the overall image representation with the full report embedding, whereas OSL enforces the similarity of a true concise diagnostic statement to be higher than its faulty opposite. The two are balanced equally in the alignment objective:

$$\mathcal{L}_{\text{align}} = 0.5 \mathcal{L}_{\text{CLIP}} + 0.5 \mathcal{L}_{\text{OSL}}. \quad (7)$$

This joint formulation ensures that embeddings preserve both global contextual alignment and fine-grained diagnostic contrast.

B.4.6 CLIP, RRG, MAE and OSL

Having integrated independently the MAE with CLIP and RRG with CLIP, we merge the optimal configurations (Secs. B.2.2 and B.3.1) of CLIP + RRG+ MAE without further ablations together with our OSL, yielding our final COLIPRI-CRM VLE. Validation results of all our final configurations are provided in Tab. B.7.

Table B.7. **COLIPRI development results.** COLIPRI-CRM and COLIPRI-CM exceed COLIPRI-CR and COLIPRI-C. In retrieval COLIPRI-CRM further exceeds COLIPRI-CM yielding a well-rounded encoder with high global task performance.

	Retrieval			Probing			Zero-shot (N)		Zero-shot (S)	
	R@1	R@5	R@10	AUPRC	AUROC	AUPRC	AUROC	AUPRC	AUROC	
COLIPRI-C	11.36	27.74	37.34	55.59	83.13	44.53	78.93	43.74	77.05	
COLIPRI-CR	16.46	33.25	41.60	57.05	83.46	48.27	79.34	45.05	77.53	
COLIPRI-CM	26.40	51.13	61.57	61.11	86.17	51.17	81.91	50.70	81.66	
COLIPRI-CRM	28.74	53.55	62.16	61.12	86.27	51.19	81.64	50.57	81.53	

B.5. Hyperparameter configurations

The final hyperparameter configurations for COLIPRI-C, COLIPRI-CR and COLIPRI-CM are provided in Tabs. B.8 to B.10. Not explicitly noted hyperparameters are ‘inherited’ from COLIPRI-C. Hyperparameters of COLIPRI-CRM are the combination of COLIPRI-C, COLIPRI-CR and COLIPRI-CM with a combination of the \mathcal{L}_{VLM} loss of the COLIPRI-CR and the \mathcal{L}_{VO} of the COLIPRI-CM model.

C. Evaluation details

C.1. Metrics

C.1.1 Retrieval metrics

Recall Given image report-pairs, we evaluate the image-to-report retrieval through using Recall @ 1/5/10. This is calculated by embedding the entire validation set or test set of image-report pairs, yielding N validation images and reports.

This yields N global image embeddings and N report embeddings, for which we calculate the similarities between all pairs, identically as during the CLIP training. Following this, we measure whether the image embedding of the actual image is i) the most similar, ii) within the five most similar or iii) within the 10 most similar images. From these results, we compute Recall@1, Recall@5, and Recall@10, which quantify the proportion of test samples for which the correct image appears among the top-1, top-5, or top-10 retrieved results, respectively. A higher recall value indicates that the learned embedding space more effectively aligns visual and textual representations, allowing relevant image-report pairs to be retrieved more reliably.

The results for report-to-image retrieval are computed analogously.

C.1.2 Classification metrics

Area under the receiver operating characteristic curve (AUROC) The AUROC metric evaluates a model’s ability to distinguish between positive and negative cases across all possible decision thresholds and is computed as the area under the curve defined by the true positive rate (sensitivity) plotted against the False Positive Rate (1 – specificity).

Table B.8. **Hyperparameters of the COLIPRI-C encoder.** Num. warm-up steps: Steps for learning rate warm-up (deducted from total steps).

Vision Encoder	
Architecture	Primus-M
Layer scale	0.1
Drop path rate	0.2
Post-attention normalisation	True
Absolute positional encoding	False
3D RoPE	True
Patch Size	$8 \times 8 \times 8$
Pooling	Multi-head attention pooling
Num. att. pooling heads	12
Attention pooling query	Mean pooling
Vision encoder init	Random
Text encoder	
Architecture	CXR-BERT ⁴
Tokeniser	Tokeniser associated with CXR-BERT
Max. token length	512
Text pooling	Multi-head attention pooling
Num. attention pooling heads	12
Att. pooling query method	Mean pooling
Training Parameters	
Input size	$160 \times 160 \times 160$
Batch size	16
Learning rate	6×10^{-5}
Weight decay	5×10^{-3}
Optimiser	AdamW
Betas	(0.9, 0.98)
Num. warm-up steps	6250
Warm-up schedule	Linear
Total num. steps	125k
Learning rate schedule	PolynomialLR
Image augmentation	Default nnU-Net augmentation
<i>Sentence Shuffle</i> aug.	True
<i>Short Sentence</i> aug. prob.	25%
Text used	<i>Findings</i>
Loss: $\mathcal{L}_{align} = \lambda_{CLIP} \cdot \mathcal{L}_{CLIP} + \lambda_{OSL} \cdot \mathcal{L}_{OSL}$	
\mathcal{L}_{CLIP}	Symmetric InfoNCE
\mathcal{L}_{OSL}	Cross-entropy
CLIP temperature \mathcal{T}	0.07
λ_{CLIP}	0.5
λ_{OSL}	0.5
Num. OSL sentence pairs	8

An AUROC of 0.5 indicates random performance, whereas a value of 1.0 represents perfect discrimination.

Area under the precision-recall curve (AUPRC) The AUPRC metric measures a model’s ability to identify positive cases across varying decision thresholds, emphasising performance on imbalanced datasets. It is computed as the area under the curve defined by precision (positive predictive value) plotted against recall (sensitivity). Unlike AUROC, which considers both positive and negative classes equally, AUPRC focuses on the model’s effectiveness in detecting the positive class, making it particularly informative when positive cases are rare, as is the case for many abnormalities. A higher AUPRC indicates that the model main-

Table B.9. **Hyperparameters of the COLIPRI-CR encoder.** The majority of hyperparameters is kept identical to COLIPRI-C, only changes and newly included hyperparameters are reported. RRG: Radiology Report Generation; OSL: Opposite Sentence Loss

Report Generator	
Architecture	EVA-02
Depth	4
Training Parameters	
Learning rate	3×10^{-5}
CapPa – Cap Probability	100% – 0%
Loss: $\mathcal{L}_{VLM} = \lambda_{CLIP} \cdot \mathcal{L}_{CLIP} + \lambda_{OSL} \cdot \mathcal{L}_{OSL} + \lambda_{RRG} \cdot \mathcal{L}_{RRG}$	
\mathcal{L}_{RRG}	Cross-entropy
λ_{RRG}	0.3

Table B.10. **Hyperparameters of the COLIPRI-CM encoder.** The majority of hyperparameters are kept identical to COLIPRI-C, only changes and newly included hyperparameters are reported. Loss is alternating every batch between \mathcal{L}_{Align} and \mathcal{L}_{VO} . MAE: Masked Autoencoder; OSL: Opposite Sentence Loss

Mask Generator	
Architecture	EVA-02
Depth	6
Training Parameters	
Learning rate	3×10^{-5}
Mask ratio	75%
Mask style	Random masking
Inclusion at last X% of training	100% (i.e., since the beginning)
Smallest spacing	1 mm
Vision encoder init.	Masked autoencoder (MAE)
Loss: \mathcal{L}_{Align} or $\mathcal{L}_{VO} = \lambda_{MAE} \cdot \mathcal{L}_{MAE}$	
λ_{MAE}	1
\mathcal{L}_{MAE}	Mean squared error (where masked)

tains strong precision even at high recall levels, reflecting its capacity to identify true positives while minimising false detections.

Because of this characteristics, we select the classification probe used for testing as the one that yields the highest AUPRC on the validation set.

C.1.3 Report generation metrics

RadBERT RadBERT [15] is a text classification BERT model trained on CT-RATE, which allows to predict class probabilities for the 18 different multi-abnormality classes of the CT-RATE dataset. We use Micro and Macro RadBERT F_1 -scores to evaluate the report generation performance on top of the encoders.

RadFact (+/-) and RadFact (+) RadFact [4] assesses the factuality of a generated report by evaluating whether each

sentence in the generated report is supported by a sentence in the reference (ground-truth) report and vice versa. This is achieved by leveraging the reasoning capabilities of GPT-4o.

Because our data differ from the X-ray reports used in the original work, we adapt RadFact’s system prompt and introduce two distinct RadFact variants: RadFact-CT (+/-) and RadFact-CT (+). RadFact-CT (+/-) evaluates both positive and negative radiological statements, while RadFact-CT (+) focuses exclusively on positive findings, excluding statements about the absences of abnormality, unremarkable observations, or normal anatomy.

In this study, we employ RadFact’s *Logical Precision* and *Logical Recall* to compute a *Logical F_1* score. The grounding and spatial reasoning capabilities of RadFact are not considered in our evaluation.

C.2. Classification linear probing

Given a pre-trained encoder, we conduct linear probing to measure the quality of our vision encoders embeddings for classifying the abnormalities labelled in CT-RATE and RAD-ChestCT. To do so, we discard the original token aggregation scheme of the vision encoder, which was aimed at aligning image and report, and instead train a new one for classification. As the best token aggregation scheme is unknown, we conduct a grid search over five different schemes and four different learning rates. The token aggregation schemes are:

1. **Average pooling:** a simple averaging across the sequence dimension.
2. **Max pooling:** a simple max-pooling across the sequence dimension.
3. **Learnt attention pooling:** an attention pooling head with a learned query token, steering how the tokens are recombined to yield the final global representation.
4. **Average attention pooling:** same as above but with the learnt query replaced by a token created through average pooling.
5. **Multi-learnt attention pooling:** As learnt attention pooling but with four learned query tokens instead of one. As we get one representation for each query, the four outputs are averaged to yield the global representation.

All of these token pooling schemes yield a global embedding which we project down through a linear layer to the 18 abnormalities annotated in CT-RATE.

The four learning rates over which we sweep are $lr \in \{3 \times 10^{-3}, 1 \times 10^{-2}, 3 \times 10^{-2}, 1 \times 10^{-1}, \}\$. As we keep the encoder frozen, we can allocate the majority of VRAM to the probes, allowing us to train all of them jointly [31].

The probes are trained using a batch size of 16, for 12.5k steps, using an SGD optimiser with momentum 0.95 and no weight decay, following a cosine annealing learning rate

schedule. As the input volumes are larger than the input size, we conduct centre-cropping of the volume, extracting a central $s \times s \times s$ crop (the same as the vision encoder’s input size s). Once training concluded, the best probe is selected based on the area under the precision-recall curve (AUPRC) values on the validation set. When using the probes for testing, the best probe on the validation set is used for evaluation on the test set, yielding the final metrics.

C.3. Zero-shot classification

Opposed to the trained classification probes of Sec. C.2 the originally trained multi-head attention pooling as well as the language-encoder and language-pooling is reused to evaluate zero-shot classification performance. In this paper we differentiate between two zero-shot classification schemes: ‘native’ and ‘short’ (Sec. A.4).

Given the language embeddings representing the presence or absence of an abnormality, a global vision embedding is extracted from a centre-crop of each image. For each of these global vision embedding the cosine similarity between the vision and the two language embeddings is calculated, the similarities are temperature-scaled (divided by 0.07), and the resulting logits are fed through a softmax to yield probabilities associated with the presence and absence of the abnormality. The probability associated with the positive embedding is used to calculate the metrics as in Sec. C.2.

C.4. Report generation

We tested the potential of our patch embeddings on the vision–language task of report generation. For the language component, we used the Qwen2.5-1B base model [42], which was not instruction-tuned to ensure fair evaluation of intrinsic alignment.

Our training recipe adheres to the LLaVA-style framework [25], where a canonical frozen vision encoder and trainable decoder paradigm is used for multimodal vision–language generation. The 3D vision backbone remains frozen throughout training to preserve pre-learned visual representations. On top of this encoder, we train both a cross-modal alignment module and the language decoder. We employ a causal language modelling loss with teacher forcing, applied to tokenised radiology reports. The optimisation objective is thus purely autoregressive, and no auxiliary objectives are introduced.

Following prior work [25, 35], we integrated vision tokens into the language space through a two-layer multilayer perceptron (MLP) projection head. We constrain supervision to the *Findings* section of the CT report. The *Findings* provide high-density, structured clinical interpretation of the CT volume, covering organ-level abnormalities and radiographic evidence. In contrast, the *Impression* section,

although often used in clinical practice, introduces redundancy without providing additional information that could be extracted from the input image. We therefore omit the *Impression* section in all experiments.

Each LLM is fine-tuned on the CT-RATE training set with a batch size of 32 for 10 epochs, with no weight decay. The maximum learning rate is 5×10^{-5} and a cosine learning rate schedule is used with a linear warm-up for 3% of the training steps. These hyperparameters were selected to maximise the RadBERT Micro- F_1 scores on the validation set.

C.5. Retrieval

Multimodal retrieval evaluate how well a model aligns visual and text representations in a shared embedding space. By retrieving the correct clinical report given an image (image-to-report retrieval), we directly measure whether the model captures clinically meaningful visual semantics and associates them with corresponding textual descriptions. In a clinical context, this task could be leveraged for retrieval-augmented generation (RAG) of reports. Analogously, retrieving an image given a report assesses similar model capabilities and could be used to visualise multiple manifestations of the reported abnormalities. Although we do not deal with unimodal retrieval in this paper (i.e., image-to-image or report-to-report), this task might also be of interest for certain applications.

Retrieval thus serves as a strong proxy for multimodal understanding and vision–language alignment. As the pre-training objectives include image–report alignment, no additional adaptation step is required for this task. Hence, the vision and text encoders with their respective pooling mechanisms are used as-is to evaluate this task.

C.6. Segmentation fine-tuning

To evaluate segmentation performance, we leverage the pre-training adaptation framework proposed in nnSSL [49], which introduces fine-tuning of pre-trained vision encoders into the well-established nnU-Net framework [20]. In particular, a longer training schedule of 1000 nnU-Net pseudoepochs (250k iterations) and a shorter training schedule of 150 nnU-Net pseudoepochs (37.5k iterations) were proposed in this paper. We leverage both to evaluate the embedding quality of our vision encoders, with details on the explicit settings available in Wald et al. [49] and the nnSSL repository⁵.

Segmentation dataset preprocessing During pre-training we trained our vision encoder on CT data that was mapped from $[-1000, 1000]$ to $[-1, 1]$ and clipped to $[-1, 1]$. However, in initial tests, we found this to yield subpar results for semantic segmentation. Consequently, we

⁵<https://github.com/MIC-DKFZ/nssl>

stick to the official nnU-Net normalisation, referred to as CTnormalisation, which clips values outside the 0.5th percentile and the 99.5th percentile before standardising to zero mean and unit variance (the standardisation statistics are computed on the whole dataset). Moreover, despite the majority of encoders trained on 2-mm isotropic spacing (with the exception of some MAEs), we chose to resample the segmentation datasets to 1-mm isotropic spacing, as this resolution is substantially closer to the median spacings the downstream datasets come with. We note that, while this shift in normalisation and spacing is not optimal and may negatively influence segmentation results, this setting still allows us to compare the performance of different models. While the spacing issue is not easily avoidable, the normalisation choice could be adapted easily in future work by preprocessing the pre-training data identically.

D. Extended results

In addition to the results presented in the main manuscript, we provide extended result tables displaying:

1. Zero-shot classification results in Tab. [D.1](#).
2. Report-generation results in Tab. [D.2](#).
3. Report-generation results for each abnormality in Sec. [D](#).
4. Segmentation results of all folds in Tab. [D.3](#).
5. Image-to-report and report-to-image retrieval including mean and median ranks in Tab. [D.4](#).
6. Segmentation and classification results highlighting the importance of initialising with MAE pre-trained weights Tab. [D.5](#).

Table D.1. **Additional zero-shot classification results** complementing Tab. 2. When conducting zero-shot classification with long-form “native” prompts, performance is slightly higher, yet within confidence intervals for our encoders. Overall, COLIPRI-CRM and COLIPRI-CM reach highest performance. **Bold** indicates best performance for that metric, or overlapping confidence intervals (CIs) with best. Prompt: prompt style; AUPRC: area under precision recall curve; AUROC: area under receiver operating characteristic curve. *Values taken from Shui et al. [37].

Model Included Classes	Prompt	CT-RATE				RAD-ChestCT			
		All abnormalities		like fVLM		All abnormalities		like fVLM	
		AUPRC	AUROC	AUPRC	AUROC	AUPRC	AUROC	AUPRC	AUROC
MI2	short	19.03	49.47	18.80	49.36	26.57	48.78	26.32	48.82
Curia	short	19.33	49.93	19.18	50.17	27.14	50.21	26.84	50.13
CT-CLIP	(own)	-	-	-	70.4*	-	63.2*		
BIUD	(own)	-	-	-	71.3*	-	62.9*		
Merlin	(own)	-	-	-	72.8*	-	62.9*		
fVLM	(own)	-	-	-	77.8*	-	68.0*		
COLIPRI-C	short	42.04 [41.1, 43.3]	75.02 [74.3, 75.9]	43.81 [42.9, 45.2]	76.25 [75.5, 77.2]	41.05 [40.6, 41.9]	68.71 [68.3, 69.2]	40.98 [40.3, 41.8]	69.12 [68.6, 69.7]
COLIPRI-CR	short	43.36 [42.4, 45.0]	75.23 [74.5, 76.1]	44.70 [43.7, 46.5]	76.41 [75.7, 77.2]	39.93 [39.3, 40.6]	67.07 [66.5, 67.8]	39.38 [38.7, 40.1]	67.30 [66.6, 68.1]
COLIPRI-CM	short	48.62 [47.2, 50.1]	79.78 [79.0, 80.6]	50.32 [48.7, 51.8]	80.52 [79.7, 81.4]	44.45 [43.7, 45.4]	72.20 [71.7, 72.8]	43.26 [42.5, 44.3]	72.05 [71.4, 72.7]
COLIPRI-CRM	short	47.53 [46.4, 49.5]	78.53 [77.8, 79.3]	49.39 [48.3, 51.3]	79.81 [79.2, 80.7]	45.15 [44.4, 45.9]	72.98 [72.4, 73.5]	44.48 [43.7, 45.4]	73.23 [72.6, 73.8]
MI2	native	19.33	49.99	19.51	49.97	26.85	49.93	27.12	49.85
Curia	native	19.54	50.27	19.80	50.46	26.94	50.29	27.23	50.24
COLIPRI-C	native	41.49 [39.7, 42.9]	75.48 [74.8, 76.2]	42.16 [40.5, 43.6]	75.74 [74.9, 76.5]	39.11 [38.4, 39.9]	66.40 [65.8, 67.0]	38.20 [37.5, 39.1]	66.34 [65.7, 66.9]
COLIPRI-CR	native	43.57 [42.0, 45.0]	75.90 [74.9, 76.7]	43.56 [42.1, 44.9]	75.77 [74.8, 76.5]	40.85 [40.2, 41.6]	67.72 [67.1, 68.3]	40.30 [39.7, 41.2]	67.86 [67.3, 68.4]
COLIPRI-CM	native	49.53 [47.7, 50.9]	80.27 [79.4, 81.0]	49.94 [48.2, 51.3]	80.44 [79.5, 81.2]	43.88 [43.2, 44.8]	70.89 [70.4, 71.4]	42.21 [41.6, 43.1]	70.42 [69.8, 71.0]
COLIPRI-CRM	native	48.78 [47.0, 50.5]	79.53 [78.5, 80.3]	49.34 [47.8, 51.0]	79.70 [78.7, 80.4]	43.84 [43.3, 44.6]	71.19 [70.7, 71.7]	42.36 [41.8, 43.2]	70.86 [70.4, 71.4]

Table D.2. **Complete report generation results.** We compare the embedding quality of our pre-trained vision encoders against available baselines when used for radiology report generation (RRG). Across most metrics, our COLIPRI models exceed the baselines. In particular, we exceed the baselines by >17 points as measured by RadBERT Macro F_1 and by >7 points when focusing on sentences about pathological findings, as measured by RadFact-CT/Logical F_1 (+/-). Note that RadFact-CT/Logical F_1 (+/-) relies aggressively on negative findings, which are very frequent and less important than positive findings (Sec. 5.3). We report median and 95% CIs based on 500 bootstrap samples. **Bold** indicates best performance for that metric, or overlapping CIs with best.

Metric	MI2	Curia	CT-CLIP	CT-FM	Merlin	COLIPRI-C	COLIPRI-CR	COLIPRI-CM	COLIPRI-CRM
Lexical metrics									
ROUGE-L	54.2 [53.1, 55.4]	54.4 [53.1, 55.5]	54.2 [53.0, 55.3]	52.4 [51.4, 53.4]	53.2 [52.1, 54.3]	55.0 [53.8, 56.1]	54.0 [53.0, 55.2]	55.0 [53.7, 56.2]	55.2 [54.1, 56.3]
BLEU-1	55.5 [54.2, 57.0]	55.1 [53.8, 56.5]	55.6 [54.3, 57.1]	57.8 [56.6, 59.1]	58.7 [57.5, 59.9]	62.8 [61.7, 63.8]	61.9 [60.8, 63.0]	63.3 [62.1, 64.5]	63.4 [62.2, 64.8]
BLEU-4	41.1 [39.8, 42.4]	40.9 [39.6, 42.3]	41.0 [39.7, 42.4]	41.2 [40.0, 42.6]	42.2 [40.9, 43.5]	44.7 [43.5, 46.0]	43.8 [42.5, 45.1]	45.0 [43.7, 46.4]	45.2 [43.8, 46.5]
METEOR	53.7 [52.6, 54.8]	53.7 [52.6, 54.9]	53.7 [52.5, 54.8]	53.5 [52.5, 54.6]	54.6 [53.6, 55.7]	57.3 [56.2, 58.4]	56.3 [55.3, 57.5]	57.6 [56.4, 58.8]	57.8 [56.6, 58.8]
Clinical metrics									
RadBERT macro F_1	14.3 [12.7, 15.9]	15.4 [13.7, 16.8]	15.3 [13.6, 17.0]	20.3 [18.7, 21.9]	21.2 [19.9, 22.6]	40.8 [39.1, 42.3]	39.8 [38.3, 41.3]	44.1 [42.6, 45.4]	44.9 [43.3, 46.4]
RadBERT micro F_1	18.7 [17.0, 20.3]	19.8 [18.1, 21.6]	19.4 [17.7, 21.1]	26.2 [24.6, 27.8]	28.9 [27.5, 30.4]	45.9 [44.4, 47.4]	45.6 [44.3, 46.8]	50.1 [48.7, 51.4]	51.0 [49.5, 52.2]
RadFact-CT/Logical F_1 (+/-)	66.5 [65.4, 67.6]	66.3 [65.3, 67.3]	68.7 [67.7, 69.6]	67.4 [66.4, 68.4]	68.2 [67.3, 69.2]	66.7 [65.6, 67.9]	66.3 [65.2, 67.3]	67.0 [66.0, 68.1]	66.9 [65.6, 68.0]
RadFact-CT/Logical F_1 (+)	12.8 [11.4, 14.2]	13.2 [11.7, 14.7]	12.8 [11.4, 14.2]	11.5 [10.5, 12.7]	11.7 [10.8, 12.7]	21.1 [19.9, 22.3]	20.7 [19.6, 21.9]	22.7 [21.7, 24.0]	22.4 [21.2, 23.6]
RadFact-CT/Logical Precision (+)	15.8 [13.7, 17.9]	15.2 [13.3, 17.4]	14.8 [13.0, 16.8]	13.9 [12.6, 15.4]	14.1 [12.9, 15.4]	24.4 [22.9, 26.0]	24.6 [23.2, 26.2]	26.9 [25.4, 28.5]	27.0 [25.4, 28.8]
RadFact-CT/Logical Recall (+)	10.8 [9.4, 12.3]	11.6 [10.2, 13.2]	11.3 [9.7, 12.7]	9.9 [8.9, 11.0]	10.1 [9.1, 11.1]	18.5 [17.1, 19.8]	17.9 [16.7, 19.1]	19.7 [18.5, 20.9]	19.1 [17.9, 20.3]

Table D.3. **Extended segmentation results.** We report the Dice similarity coefficient (DSC) of our pre-trained encoders and baselines for each fold of a five-fold cross-validation on all datasets.

	LiTS				Lung				HVS				KITS23						
	0	1	2	3	4	Avg.	0	1	2	3	4	Avg.	0	1	2	3	4	Avg.	
References (250k steps)																			
nnU-Net def.	83.30	77.49	81.07	83.14	75.46	80.09	66.31	69.33	66.38	79.52	70.03	70.32	70.36	69.78	67.67	69.51	64.59	68.38	86.41
nnU-Net ResEnc-L	83.21	79.30	83.04	83.71	78.75	81.60	67.58	70.52	66.46	77.31	69.83	70.34	69.54	67.98	67.06	69.09	64.98	67.73	88.60
Primus-M (37.5k steps)																			
From scratch	78.24	71.03	74.27	76.20	72.22	74.39	72.10	53.60	61.78	55.39	70.84	62.74	67.25	65.83	64.90	64.05	61.34	64.67	79.34
MAE	81.79	78.96	81.50	82.97	76.15	80.27	74.03	57.26	65.03	67.75	71.52	67.12	68.78	67.44	67.23	68.02	64.01	67.10	85.03
COLIPRI-C	77.96	76.30	74.94	81.05	73.59	76.77	69.19	54.66	63.59	70.96	71.04	65.89	67.08	65.37	65.47	63.74	61.55	64.64	82.31
COLIPRI-CR	80.01	76.14	76.77	78.65	73.87	77.09	73.49	49.34	62.15	70.80	70.83	65.32	66.40	66.73	65.84	64.48	61.95	65.08	81.06
COLIPRI-CM	84.19	78.63	78.19	83.17	75.66	79.97	73.95	64.99	67.50	66.54	70.74	68.74	67.78	67.67	67.79	66.28	63.38	66.58	85.59
COLIPRI-CRM	83.81	79.47	80.08	83.19	75.77	80.46	72.50	63.72	71.09	66.36	71.27	68.98	69.67	68.23	67.14	67.05	67.05	85.77	85.60
Primus-M (250k steps)																			
From scratch	80.77	78.11	81.20	82.42	76.23	79.75	72.79	62.93	63.98	73.07	72.79	69.11	67.88	65.59	65.33	65.78	62.13	65.34	86.94
MAE long	84.72	76.63	81.92	83.39	74.96	80.32	76.18	62.38	66.83	61.24	70.70	67.46	69.02	67.38	65.12	65.51	61.59	65.73	88.10
COLIPRI-CRM long	84.03	79.63	82.58	83.57	75.72	81.11	75.70	59.49	65.51	66.53	70.59	67.56	68.62	67.74	67.14	66.11	62.50	66.42	88.65

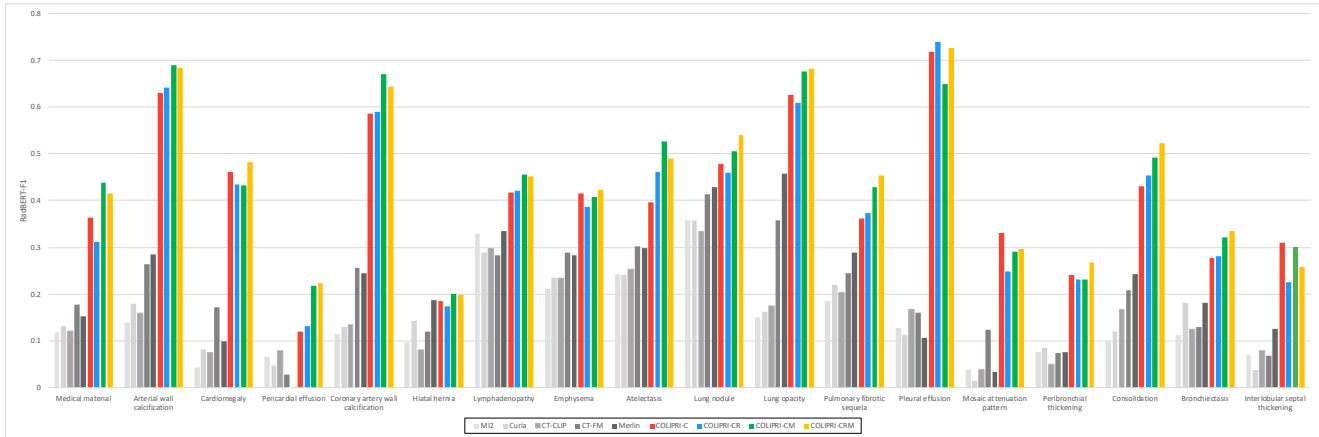


Figure D.1. **Abnormality-wise report generation results.** Additional to the macro and micro F_1 -Scores across abnormalities (Tab. D.2), we report abnormality-wise RadBERT- F_1 scores.

Table D.4. **Extended retrieval results.** Additional retrieval results on the CT-RATE test set. We present the report-to-image retrieval results after deduplication of duplicate reports and removal of head CT cases ($N = 1493$), and image-to-report retrieval after removal of head CTs ($N = 1551$).

Retrieval direction	Model	Recall			Rank	
		R@1	R@5	R@10	Median	Mean
Report to image	CT-CLIP	-	2.90	5.00	-	-
	COLIPRI-C	4.49	13.46	19.69	74	198.19
	COLIPRI-CR	7.23	19.36	26.99	47	175.53
	COLIPRI-CM	14.53	34.16	45.34	13	68.49
	COLIPRI-CRM	15.27	35.10	46.01	13	73.56
Image to report	COLIPRI-C	2.58	9.48	14.96	107	218.17
	COLIPRI-CR	4.71	13.93	20.76	69	184.37
	COLIPRI-CM	10.57	26.50	37.52	23	76.08
	COLIPRI-CRM	11.54	29.08	40.10	20	79.82

Table D.5. **Effect of MAE initialisation.** MAE initialisation and continued MAE training drives segmentation performance. When not initialising the COLIPRI-CM vision encoder with MAE pre-trained weights, COLIPRI-CM is unable to achieve reach segmentation performance. Instead it yields similar performance as the COLIPRI-C encoder, which trains without the MAE objective.

Datasets Configuration	Segmentation				Zero-shot (S) CT-RATE	
	LiTS	Lung	HSV	KiTS23	AUPRC	AUROC
From scratch	74.39	62.74	64.67	78.90	-	-
COLIPRI-C	76.77	65.89	64.64	81.02	43.74	77.05
COLIPRI-CM	79.97	68.74	66.58	86.03	50.70	81.66
w/o MAE init	76.87	63.11	64.53	79.82	45.53	78.18
Δ	-3.10	-5.63	-2.05	-6.21	-5.17	-3.48

E. Prompts and exemplary reports

E.1. Prompt to translate reports from Turkish to English

"""You are a board-certified radiologist-translator.
Translate the Turkish radiology report contained inside a single `<report> ... </report>` element into fluent, precise English.

```
#####
##  OUTPUT | COPY THIS SHAPE EXACTLY
#####
**1. Clinical Information**
English text here.
```

```
**2. Technique**
English text here.
```

```
**3. Findings**
English text here.
```

```
**4. Impression**
English text here.
```

- **The four numbered headings must stay exactly as above and remain in bold.**
- If any section is empty, whitespace, or literally `\nan`, write Not provided. (plain text, **not** bold) under that heading.
- Do **NOT** output anything outside these four labelled sections.
- No bullet characters (., {, *, etc.) or markdown lists inside the body text.

```
#####
##  INPUT
#####
You will receive one well-formed XML block:
<report>
  <clinical_information>...</clinical_information>
  <technique>...</technique>
  <findings>...</findings>
  <impression>...</impression>
</report>
#####
##  STYLE RULES
#####
• Literal, complete translation | no omissions, additions, or summaries.
• Concise, objective radiology tone (passive voice preferred).
• Use RSNA / ACR terminology; convert decimal commas to periods (7,5 mm → 7.5 mm).
• Expand abbreviations on first mention: \CT pulmonary angiography (CTPA)".
• Preserve original sentence order and punctuation.
```

```
#####
##  REQUIRED GLOSSARY | replace the Turkish term with the English term verbatim
#####
buzlu cam göründüsü          → ground-glass opacity
plevral efüzyon              → pleural effusion
septal kalınlaşma             → interlobular septal thickening
konsolidasyon                  → consolidation
akciğer nodülü                → pulmonary nodule
retiküler opasiteler          → reticular opacities
bronşiektazi                  → bronchiectasis
hiler lenfadenopati           → hilar lymphadenopathy
mediastinal şift                → mediastinal shift
trakea orta hatta              → trachea is midline
perikardiyal efüzyon           → pericardial effusion
şüpheli kitle                  → suspicious mass
subplevral bant                  → subpleural band
havayolu duvar kalınlaşması      → airway wall thickening
lenf bezisi büyümesi            → lymph-node enlargement
ateşli infiltrasyon              → inflammatory infiltration
atelektazi                      → atelectasis
bal peteği görünümü            → honeycombing pattern
fibrotik değişiklikler          → fibrotic changes
amfizem                           → emphysema
tomurcuklanmış ağaç                → tree-in-bud pattern
kontrastsız                      → non-contrast enhanced
kontrast verilmenden             → non-contrast enhanced
"""

```

E.2. Prompt to structure *Findings* sections into different subsections

```
"""You are a radiology report editor.
Restructure a non-contrast chest CT report (supplied in four free-text blocks)
into the fixed template below **without altering a single medical fact**.
----- INPUT -----
The incoming text always uses these bold labels:
**Clinical Information:** ...
**Technique:** ...
**Findings:** ...
**Impression:** ...
----- OUTPUT -----
Copy this skeleton exactly. Section and subsection titles must be **bold** and end
with a colon. After each colon insert one space, then the content or the fallback line.
**1. Clinical Information:** ...
...
**2. Technique:** ...
...
**3. Comparison:** ...
... ← If prior imaging referenced; else: No prior imaging available for comparison.
**4. Findings:** ...
**4.1 Image Quality:** ...
... ← If no limitations: Diagnostic image quality. No significant artifacts noted.
**4.2 Lungs and Airways:** ...
... ← If no pulmonary findings: No pulmonary abnormalities detected.
**4.3 Pleura:** ...
... ← If no pleural findings: Pleura unremarkable.
**4.4 Mediastinum and Hila:** ...
... ← If no findings: Mediastinal and hilar structures unremarkable.
**4.5 Cardiovascular Structures:** ...
... ← If no findings: Cardiovascular structures unremarkable.
**4.6 Bones and Soft Tissues:** ...
... ← If no findings: No osseous or soft-tissue abnormalities detected.
**4.7 Tubes, Lines, and Devices:** ...
... ← If none present: No tubes or devices identified.
**4.8 Upper Abdomen:** ...
... ← If unremarkable or not imaged: No upper-abdominal abnormalities detected.
**5. Impression:** ...
... ← If missing: No impression provided.
----- EDITING RULES -----
• Zero-omission: every medical statement from the original \Findings" and \Impression"
  MUST reappear once (and only once) in an appropriate subsection.
• Do not add, delete, combine, or reinterpret abnormalities.
• Re-phrase into concise, passive radiology English (RSNA/ACR style).
• If a section/subsection is entirely absent, insert the exact fallback line.
• No lists, bullets, metadata, or commentary|return only the final formatted report.
After drafting, mentally cross-check that every clinical phrase from the original is present.
Begin when you receive the four-block input.
"""

```

E.3. Prompt to extract positive and negative findings

You are an AI assistant that makes radiology reports more succinct. These reports are being used to train a 3D CLIP-style deep learning model. You will be given the full findings section. You will extract, for each of the 8 sections in the findings text, a list with negative findings and a list with positive findings.

In the first list, you must collect a summarized sentence for each negative finding mentioned. For example, a sentence like "Esophagus is within normal limits. In the sections passing through the upper part of the abdomen, the bilateral adrenal glands appear natural. No significant pathology was detected in the abdominal sections." must be mapped to a list like ["Normal esophagus.", "Natural bilateral adrenal glands.", "No abdominal pathologies."]. The exact sentences must be short but maintain their core message. Positive findings are not allowed in this list and have to be ignored.

In the second list you must summarize only the positive findings that are denoted. In this version sentences like 'The heart and mediastinal vascular structures have a natural appearance', 'Esophagus is within normal limits.', 'No occlusive pathology was detected in the trachea and both main bronchi.' or 'Trachea and main bronchi are open.' have to be left out. When positive (pathological) findings are mentioned, summarize them very briefly. E.g. a sentence like 'atypical infiltration areas of septal thickenings are observed in places' can be summarized as 'Septal thickenings.'. Similarly as before create a list of short sentences about positive abnormalities ["Septal thickenings.", "Multiple lung nodules.", ...]. Make sure the sentences you create are a statement and less of a description, like how someone would search for the case as opposed to how one would describe it in a findings report.

Ignore all information that cannot possibly be predicted from the corresponding single image or provided clinical information section. Any comparison or reference to prior imaging must be ignored from the output. Do not output findings about how the image was acquired.

Output this in JSON format with one key for each of the eight sections. Each section is a mapping from section name (e.g. "image quality" or "cardiovascular structures") to the "negative findings" and "positive findings" lists. This is the structure:

```
{
  "image_quality": {
    "negative_findings": [
      ...
    ],
    "positive_findings": [
      ...
    ],
    "lungs_and_airways": {
      ...
    },
    ...
  }
}
```

E.4. Exemplary structured, shortened, categorised report

```

"shortened_findings": {
  "bones_and_soft_tissues": {
    "negative_findings": [],
    "positive_findings": [
      "Osteophytes on thoracic vertebrae."
    ]
  },
  "cardiovascular_structures": {
    "negative_findings": [
      "Normal thoracic aorta diameter.",
      "Normal heart contour and size.",
      "No pericardial effusion or thickening."
    ],
    "positive_findings": [
      "Ventral collaterals in anterior left chest.",
      "Collapsed left subclavian vein.",
      "Calcified plaques in aortic arch."
    ]
  },
  "image_quality": {
    "negative_findings": [
      "No significant artifacts."
    ],
    "positive_findings": []
  },
  "lungs_and_airways": {
    "negative_findings": [
      "Trachea and main bronchi are open."
    ],
    "positive_findings": [
      "Linear atelectasis in lung parenchyma.",
      "Subsegmental atelectasis in right middle lobe.",
      "Airway wall thickening with tree-in-bud pattern.",
      "Minimal peribronchial consolidation."
    ]
  },
  "mediastinum_and_hila": {
    "negative_findings": [
      "Normal major vascular structures.",
      "No lymph node enlargement."
    ],
    "positive_findings": []
  },
  "pleura": {
    "negative_findings": [
      "Pleura unremarkable."
    ],
    "positive_findings": []
  },
  "tubes_lines_and_devices": {
    "negative_findings": [
      "No tubes or devices identified."
    ],
    "positive_findings": []
  },
  "upper_abdomen": {
    "negative_findings": [
      "No liver space-occupying lesion.",
      "Normal bilateral adrenal glands."
    ],
    "positive_findings": [
      "Atrophic left kidney."
    ]
  }
}

```

Figure E.1. **Example of a structured, shortened and categorised report.** By having the sentences shortened, we can enable our *short sentence* augmentation. By structuring the report into eight different semantic groups and into *positive findings* and *negative findings*, we enable the Opposite Sentence Loss (OSL). This processing allows us to a) create simple negations of *positive findings* creating pairs of sentences where the *positive findings* should be more similar to the cases image embedding, and b) identify whether a case has **no positive findings** for a certain semantic group (here *image quality*, *pleura*, *mediastinum and hila*, *tubes lines and devices*), which enables the use of *positive findings* and their negation of other reports to create sentence pairs where the negation should be more similar to the image embedding.